Exploring Energy Landscapes: From Molecules to Nanodevices

Objective: to exploit stationary points (minima and transition states) of the PES as a computational framework (*J. Phys. Chem. B*, **110**, 20765, 2006):

- Basin-hopping for global optimisation (*J. Phys. Chem. A*, **101**, 5111 1997)
- Basin-sampling for global thermodynamics (*J. Chem. Phys.*, **124**, 044102, 2006)
- Discrete path sampling for global kinetics (*Mol. Phys.*, **100**, 3285, 2002)

For small molecules (left), all the relevant stationary points and pathways can be located. Larger systems (right) require appropriate sampling.

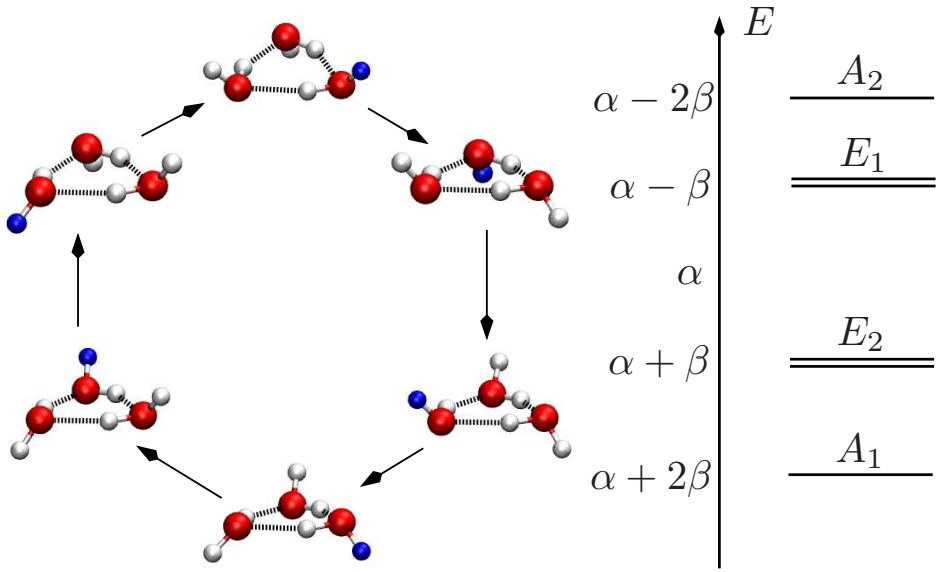

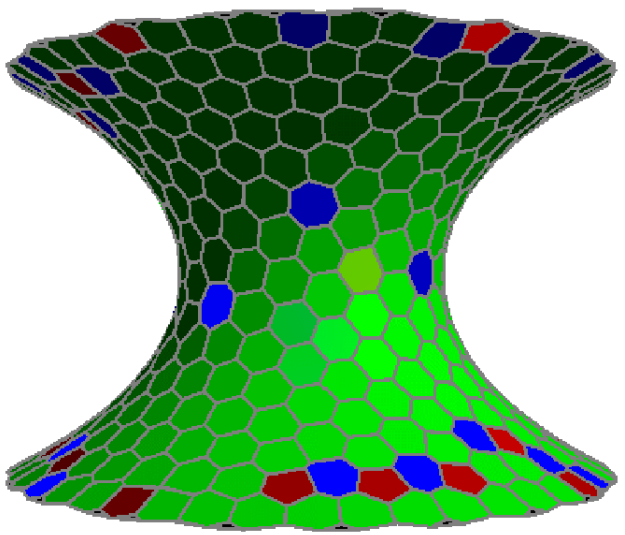

Disconnectivity Graphs of 'Funnelled' Landscapes

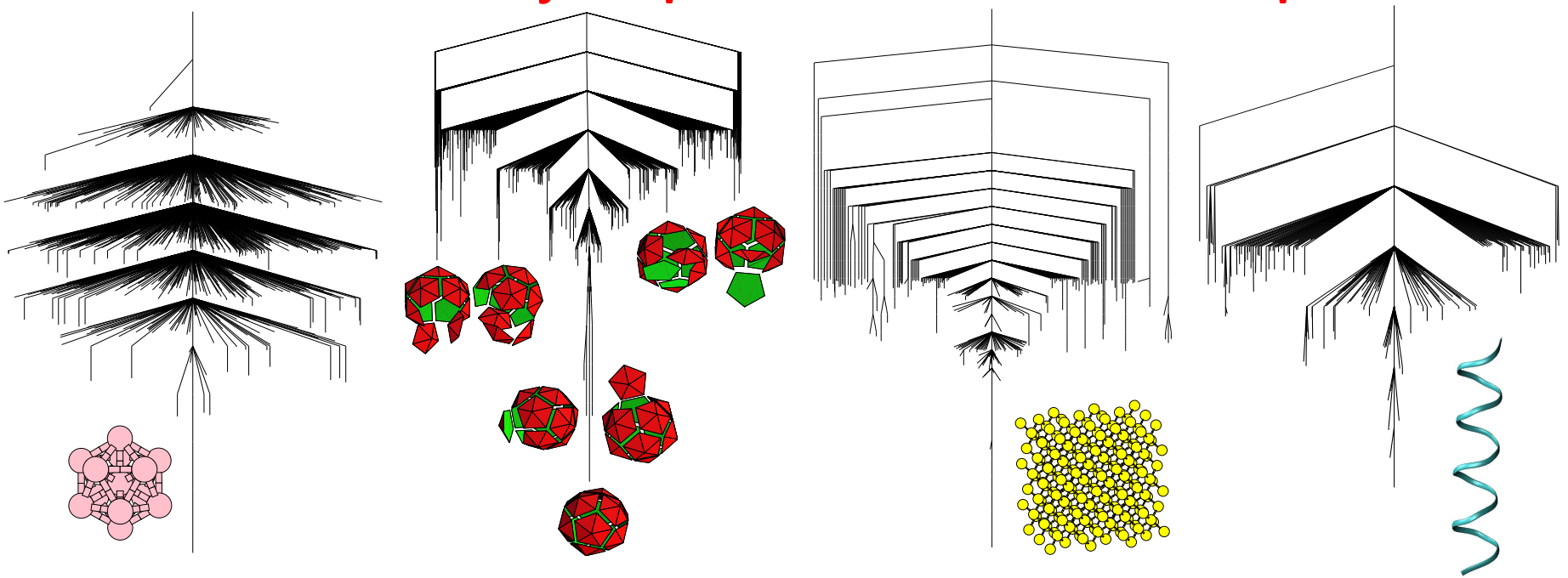

The nonrandom searches that result in magic number clusters, crystallisation, self-assembly, and protein folding are associated with a 'palm tree' organisation of the potential energy landscape (*Phil. Trans. Roy. Soc. A*, **363**, 357, 2005).

This 'funnelling' pattern has been verified for various structure-seeking systems, including the LJ_{13} cluster, icosahedral shells composed of pentagonal and hexagonal pyramids, crystalline (Stillinger-Weber) silicon, and the polyalanine ala_{16}. Large systems can exhibit relatively simple phenomenology.

Broken Ergodicity: LJ_{38} (*Phys. Rev. E*, **60**, 3701, 1999)

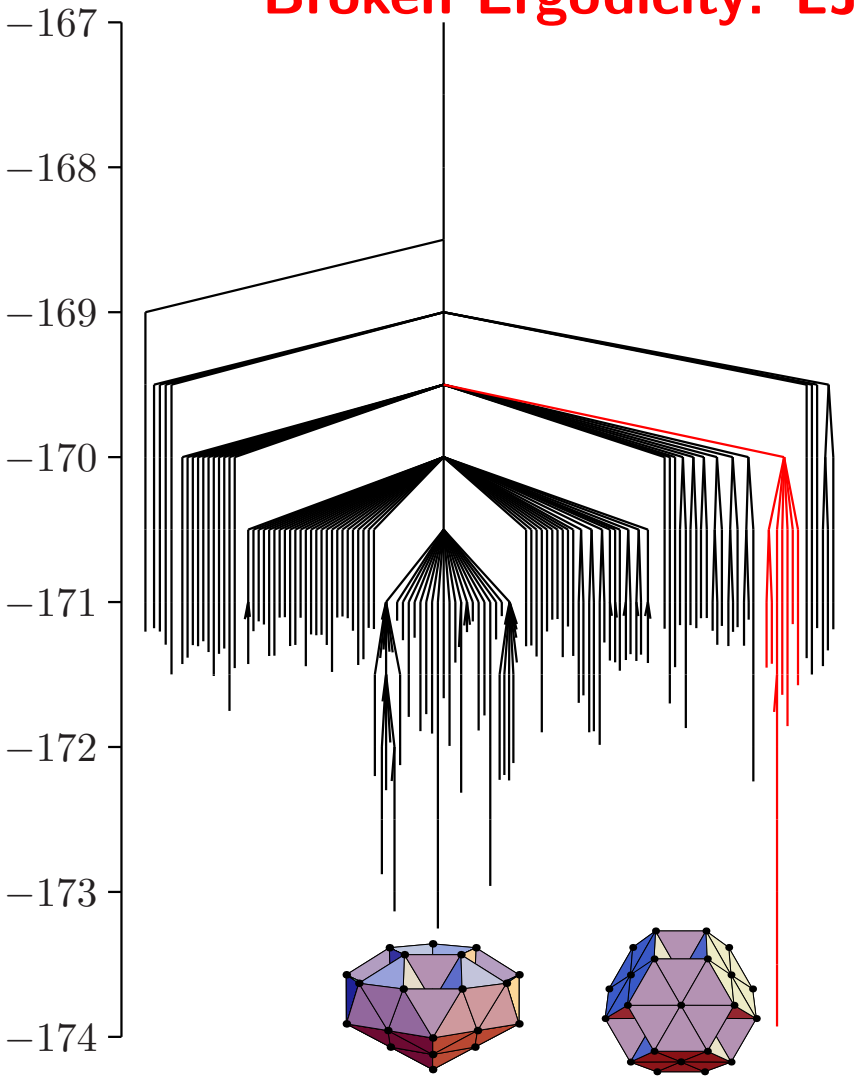

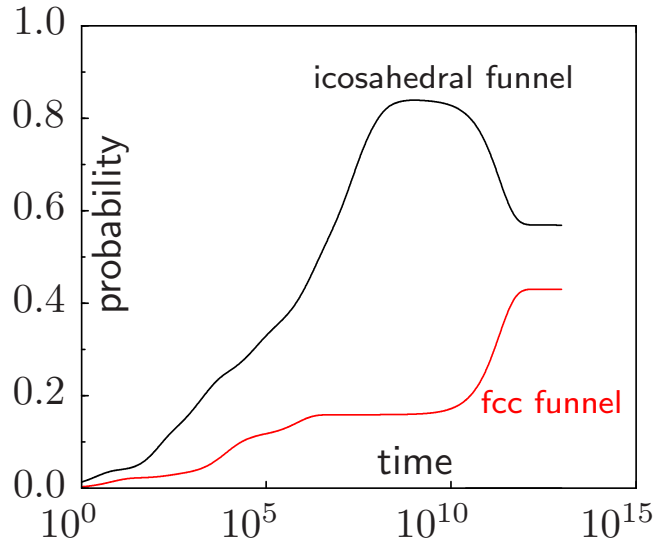

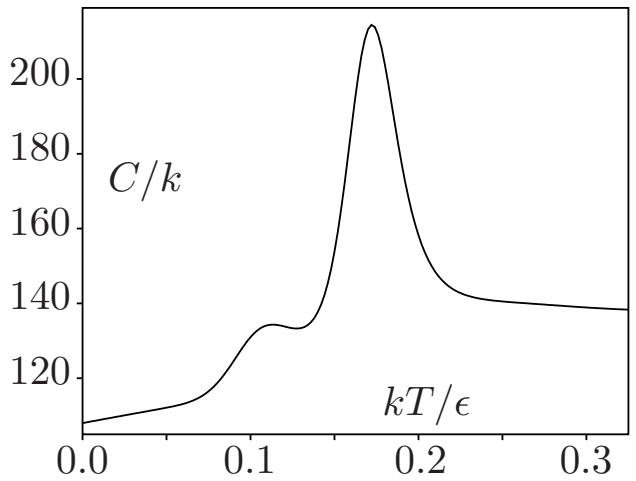

LJ_{38} exhibits a double funnel due to competition between icosahedral and truncated octahedral morphologies. The interconversion rate for Ar_{38} is calculated as $55\,s^{-1}$ at 14 K where a solid-solid transition occurs.

Basin-Hopping Global Optimisation: Structure Prediction

Transform the surface into basins of attraction: $\widetilde{E}(\mathbf{X}) = \min E(\mathbf{X})$.

Exploring $\widetilde{E}(\mathbf{X})$ using Monte Carlo steps, following Li and Scheraga (*PNAS*, **84**, 6611, 1987), produced the lowest known minima for all LJ$_n$ with $n \leq 110$ (*J. Phys. Chem. A*, **101**, 5111, 1997).

The transformation modifies both kinetics and thermodynamics.

Fortran code (`GMIN`) and database of structures: http://www-wales.ch.cam.ac.uk.

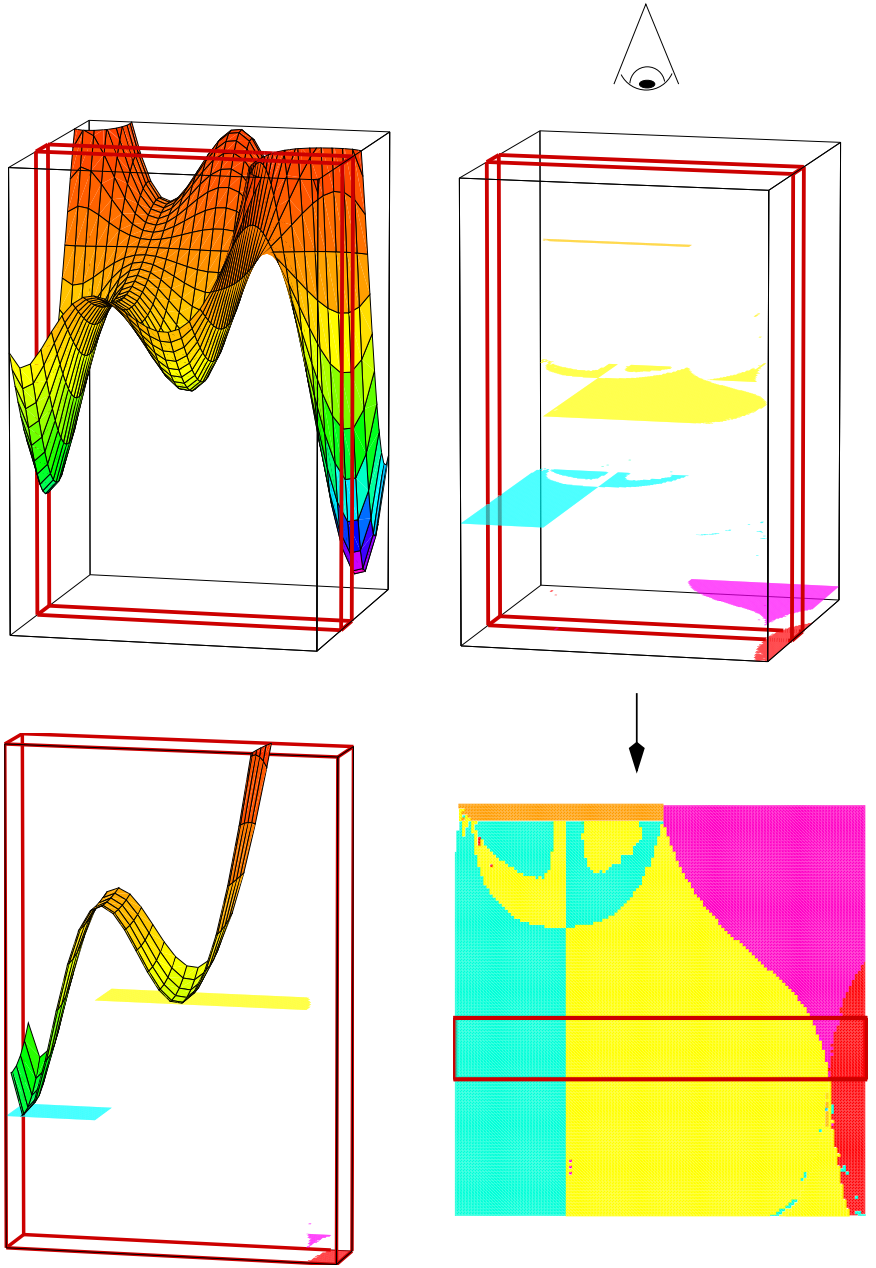

Examples from the Cambridge Cluster Database Archives

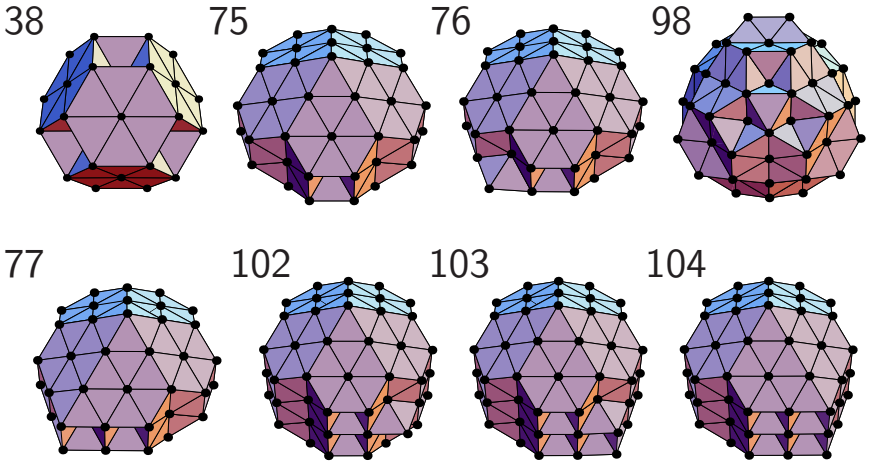

Non-icosahedral Lennard-Jones Clusters

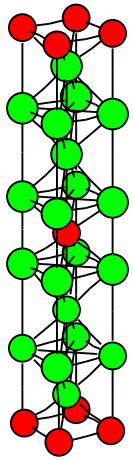

Binary LJ unit cell

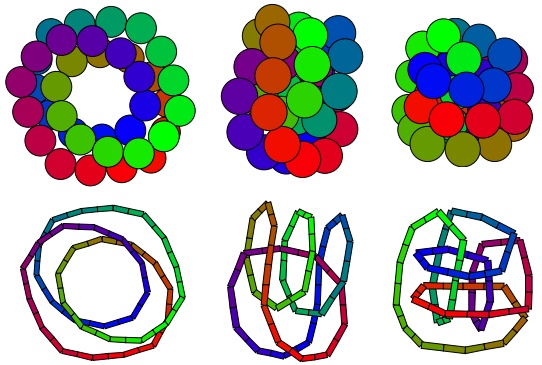

Stockmayer

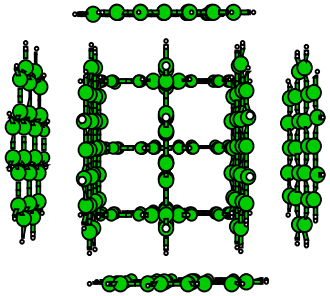

corronene$_{10}$

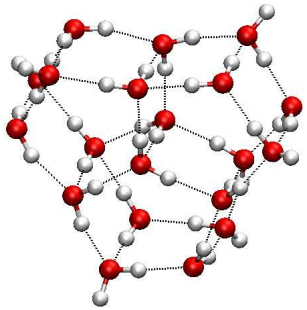

$(H_2O)_{20}$

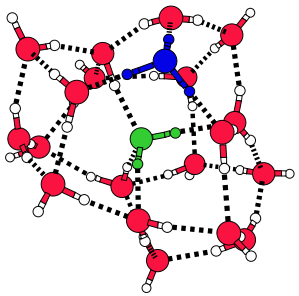

$H_3O^+(H_2O)_{20}$ Eigen

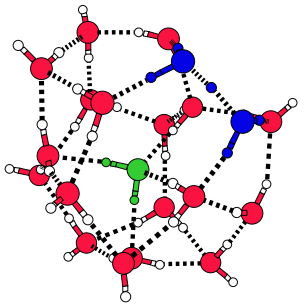

$H_3O^+(H_2O)_{20}$ Zundel

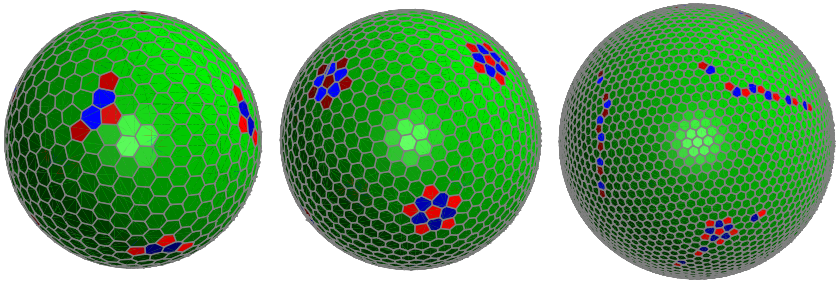

Thomson problem

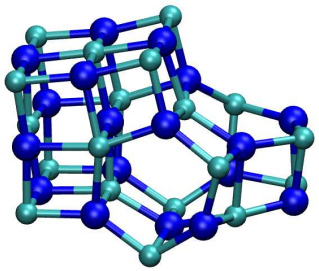

$(NaCl)_{18}Na^+$

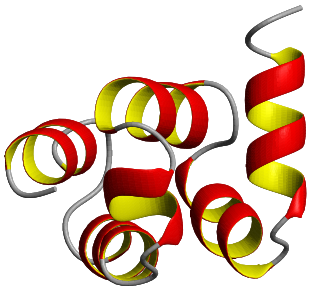

HYPA/FBP11

Transmembrane Oligomers of Aβ_{1-42} (*JACS*, **132**, 13300, 2010)

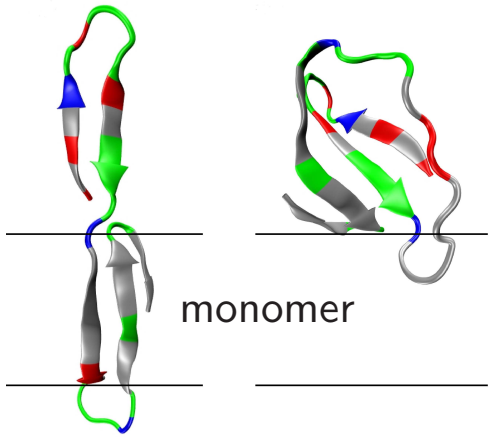

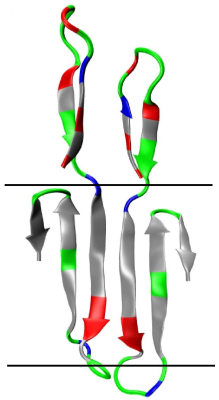

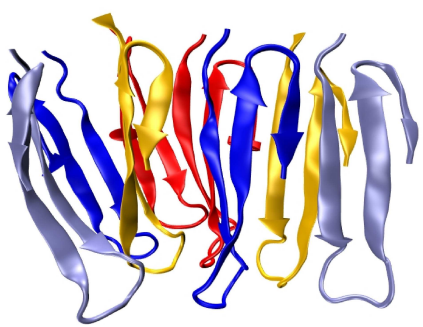

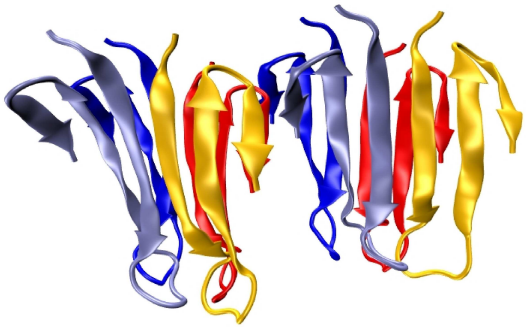

Aβ_{1-42} oligomers up to the octamer were investigated using CHARMM19 with the implicit membrane potential IMM1.

A basin-hopping/parallel tempering scheme with exchanges between basin-hopping runs at different temperatures was used, together with intra- and intermolecular coordinate moves for the peptides.

The most favourable monomer transmembrane structure has residues 17 to 42 inserted in the membrane. The most stable octamer structures can be viewed as displaced tetramers composed of two or three β-sheets.

Influenza Virus Hemagglutinin (*J. Virology*, **84**, 11802, 2010)

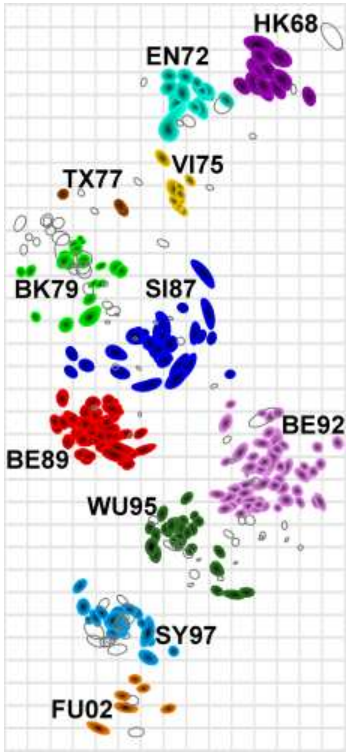

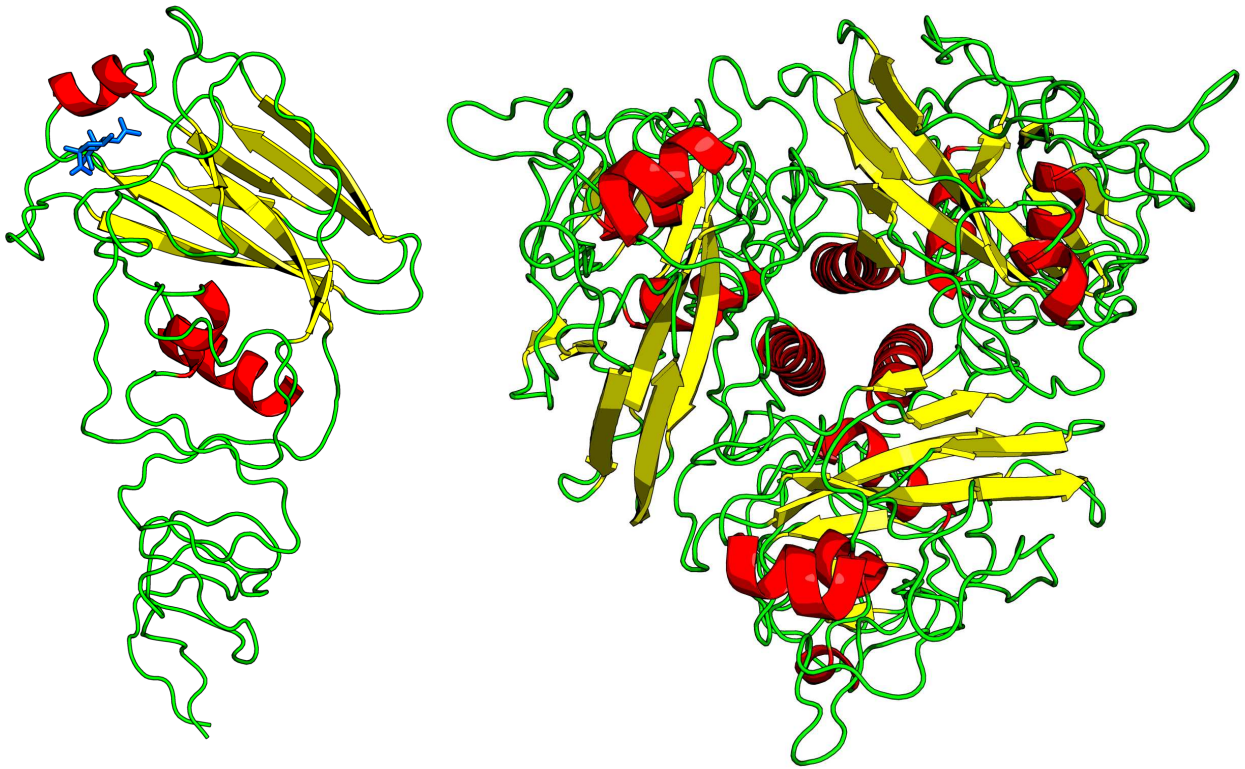

Influenza virus is a variable pathogen, causing problems for vaccination.

Antigenic shift of the hemagglutinin glycoprotein, which binds sialic acid at the cell surface, produces pandemics. Antigenic drift gives rise to epidemics.

Crystal structure is known for HK68 (H3N2). The single TY155 mutation, from threonine to tyrosine led to a cluster transition from HK68.

Discrete Path Sampling (*Mol. Phys.*, **100**, 3285, 2002; **102**, 891, 2004).

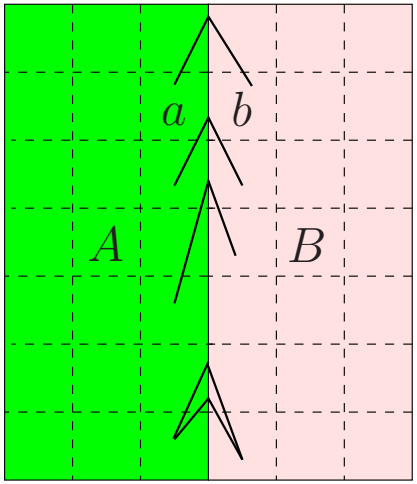

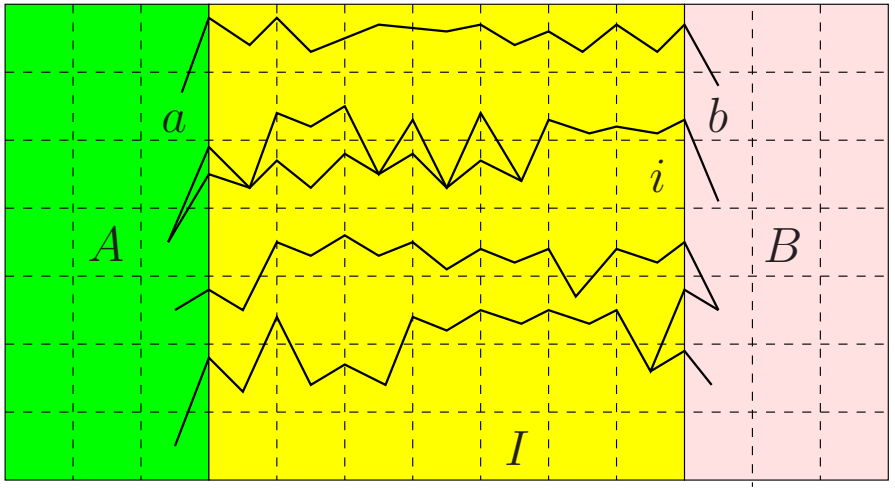

no intervening minima

$$\frac{p_a(t)}{p_{a'}(t)} = \frac{p_a^{\rm eq}}{p_{a'}^{\rm eq}} \qquad \dot{p}_i(t) = 0 \qquad \frac{p_b(t)}{p_{b'}(t)} = \frac{p_b^{\rm eq}}{p_{b'}^{\rm eq}}$$

Phenomenological $A \leftrightarrow B$ rate constants can be formulated as sums over discrete paths, defined as sequences of local minima and the transition states that link them, weighted by equilibrium occupation probabilities, $p_b^{\rm eq}$:

$$k_{AB}^{\rm SS} = \frac{1}{p_B^{\rm eq}} \sum_{a \leftarrow b} P_{ai_1} P_{i_1 i_2} \cdots P_{i_{n-1} i_n} P_{i_n b} \tau_b^{-1} p_b^{\rm eq} = \frac{1}{p_B^{\rm eq}} \sum_{b \in B} \frac{C_b^A p_b^{\rm eq}}{\tau_b},$$

where $P_{\alpha\beta}$ is a branching probability and C_b^A is the committor probability that the system will visit an A minimum before it returns to the B region.

Discrete Path Sampling (*Int. Rev. Phys. Chem.*, **25**, 237, 2006)

Discrete path sampling is a framework for growing kinetic transition networks of stationary points to describe global kinetics (*Mol. Phys.*, **100**, 3285, 2002).

The kinetic analysis involves a Markov assumption for transitions between local minima, which can be lumped recursively. Additional approximations come from incomplete sampling, and the densities of states and transition state theory used to describe the local thermodynamics and kinetics.

Rate constants are calculated using graph transformation, where minima, x, are removed deterministically, and the branching probabilities, $P_{\gamma\beta}$, and waiting times in adjacent minima, τ_β, are renormalised: (*JCP*, 124, 234110, 2006)

$$P'_{\gamma\beta} = P_{\gamma\beta} + P_{\gamma x}P_{x\beta}\sum_{m=0}^{\infty} P_{xx}^m = P_{\gamma\beta} + \frac{P_{\gamma x}P_{x\beta}}{1-P_{xx}}, \qquad \tau'_\beta = \tau_\beta + \frac{P_{x\beta}\tau_x}{1-P_{xx}}.$$

Once all the intervening states are removed we have the committor probabilities and rate constants, with $p_B^{\rm eq}k_{AB} = \sum_{b\in B} p_b^{\rm eq}/\mathcal{T}_{Ab} = \sum_{b\in B} P_{Ab}^{\rm F}p_b^{\rm eq}/\tau_b^{\rm F}$.

Discrete Path Sampling Examples II: Biomolecules

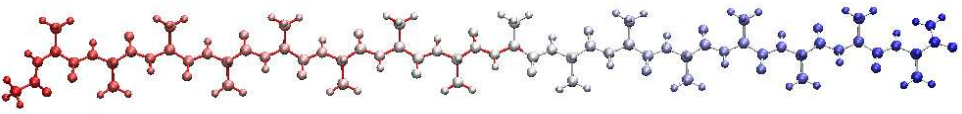

Ala_{16}

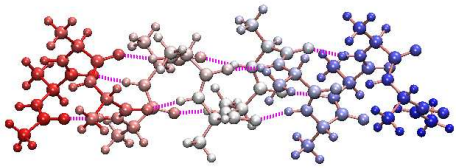

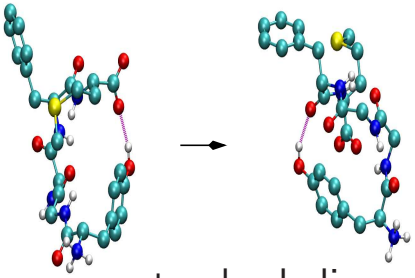

met-enkephalin

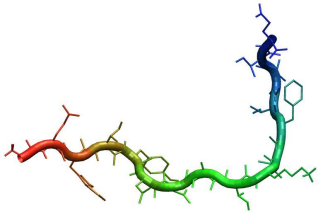

GB1
hairpin

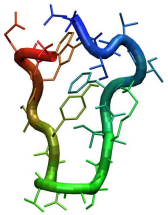

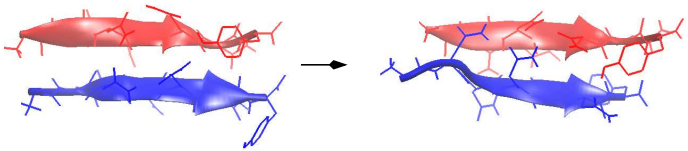

GNNQQNY

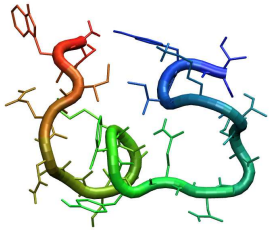

beta3s

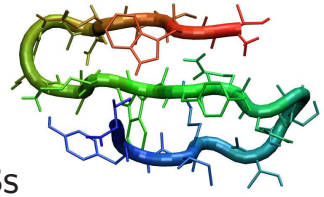

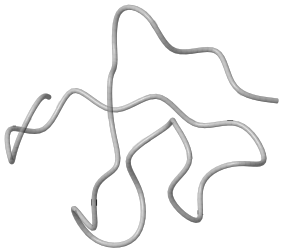

villin

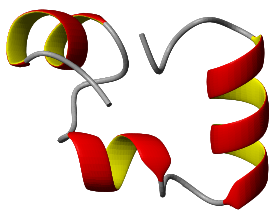

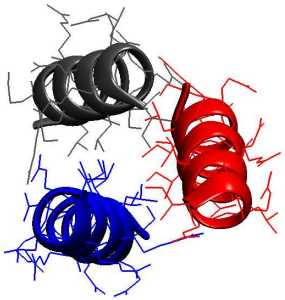

ccbeta

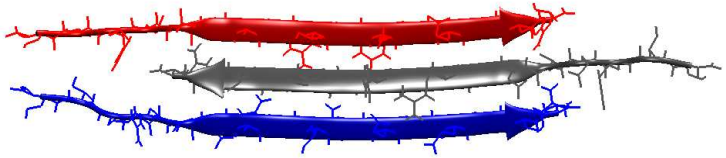

NtrC

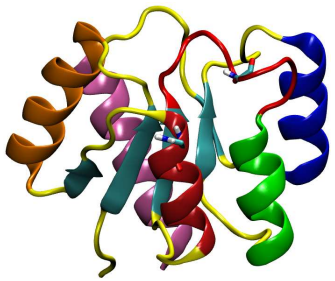

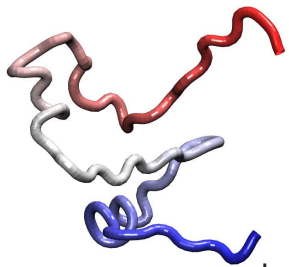

1UAM
trefoil knot

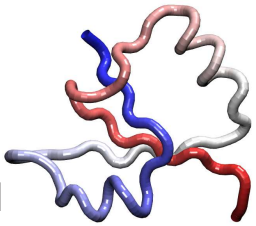

Geometry Optimisation

Minimisation: Nocedal's algorithm, LBFGS, with line searches removed.

Transition states: single-ended searches use hybrid eigenvector-following (*Phys. Rev. B*, **59**, 3969, 1999; *Chem. Phys. Lett.*, **341**, 185, 2001), double-ended searches use the doubly-nudged elastic band approach (*J. Chem. Phys.*, **120**, 2082, 2004).

The `GMIN` (global optimisation), `OPTIM` (transition states and pathways) and `PATHSAMPLE` (discrete path sampling) programs are available under the Gnu General Public License.

- Interfaces to many electronic structure codes are included.
- Current svn tarball image: http://www-wales.ch.cam.ac.uk

Benchmarks for comparing new methods:

- http://www-wales.ch.cam.ac.uk/tsbenchmarks.html Peptide examples
- http://theory.cm.utexas.edu/benchmarks/index.html OptBench test suite

THE JOURNAL OF CHEMICAL PHYSICS **135**, 034108 (2011)

Simulating structural transitions by direct transition current sampling: The example of LJ_{38}

Massimiliano Picciani,[1,a)] Manuel Athènes,[1] Jorge Kurchan,[2] and Julien Tailleur[3]
[1]*CEA, DEN, Service de Recherches de Métallurgie Physique, F-91191 Gif-sur-Yvette, France*
[2]*CNRS; ESPCI, 10 rue Vauquelin, UMR 7636 PMMH, 75005 Paris, France*
[3]*School of Physics of Astronomy, SUPA, University of Edinburgh, The King's Buildings, Mayfield Road, EH9 3JZ Edinburgh, United Kingdom*

(Received 2 March 2011; accepted 21 June 2011; published online 20 July 2011)

Another attempt to study the transitions between the two funnels of LJ_{38} relies on the use of transition path sampling.[33] Because of the number of metastable states separating the two main basins, the traditional shooting and shifting algorithm failed here, despite previous success for smaller LJ clusters.[39] The authors thus developed a two-ended approach which manages to successfully locate reaction paths between the two basins: they started from a straight trial trajectory linking the two minima, and obtained convergence towards trajectories of energies similar to those obtained in the discrete path sampling approach.[33] Although the authors point out the lack of ergodicity in the sampling within their approach and the sensitivity on the "discretization" of the trajectories, this is nevertheless a progress and the main drawback remains the high computational cost (the work needed 10^5 h of central processing unit (cpu) time) to obtain such converged trajectories. In contrast, the simulations we present below required less than 10^2 h of cpu time.

A Knotted Protein (*PLoS Comput. Biol.*, **6**, e1000835, 2010)

Quasi-Continuous Interpolation (*JCTC*, **8**, 5020, 2012)

The tRNA methyltransferase protein 1UAM contains a deep trefoil knot (right).

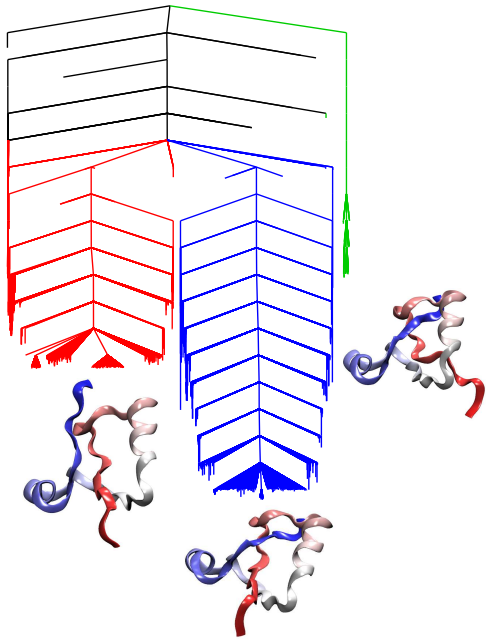

The folding pathway exhibits two slipknot-type steps for a truncated (residues 78–135) Gō model using an associated memory Hamiltonian and initial QCI.

The QCI potential preserves the covalent bonding framework, with short-range repulsion between unconstrained atoms. An internal minimum for atoms α and β between images i and j occurs if

$$[d^{ij}_{\alpha\beta}(\theta)]^2 = \frac{\left|\mathbf{r}^i_\alpha - \mathbf{r}^i_\beta\right|^2 \left|\mathbf{r}^j_\alpha - \mathbf{r}^j_\beta\right|^2 - \left[\left(\mathbf{r}^i_\alpha - \mathbf{r}^i_\beta\right)\cdot\left(\mathbf{r}^j_\alpha - \mathbf{r}^j_\beta\right)\right]^2}{\left|\mathbf{r}^i_\alpha - \mathbf{r}^i_\beta - \mathbf{r}^j_\alpha + \mathbf{r}^j_\beta\right|^2}.$$

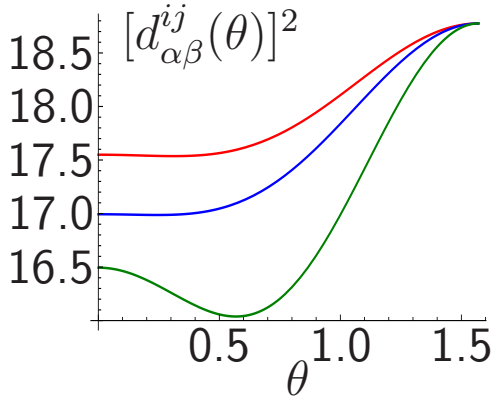

Coarse-Grained Models (*PCCP*, **11**, 1970, 2009; *ACS Nano*, **4**, 219, 2010)

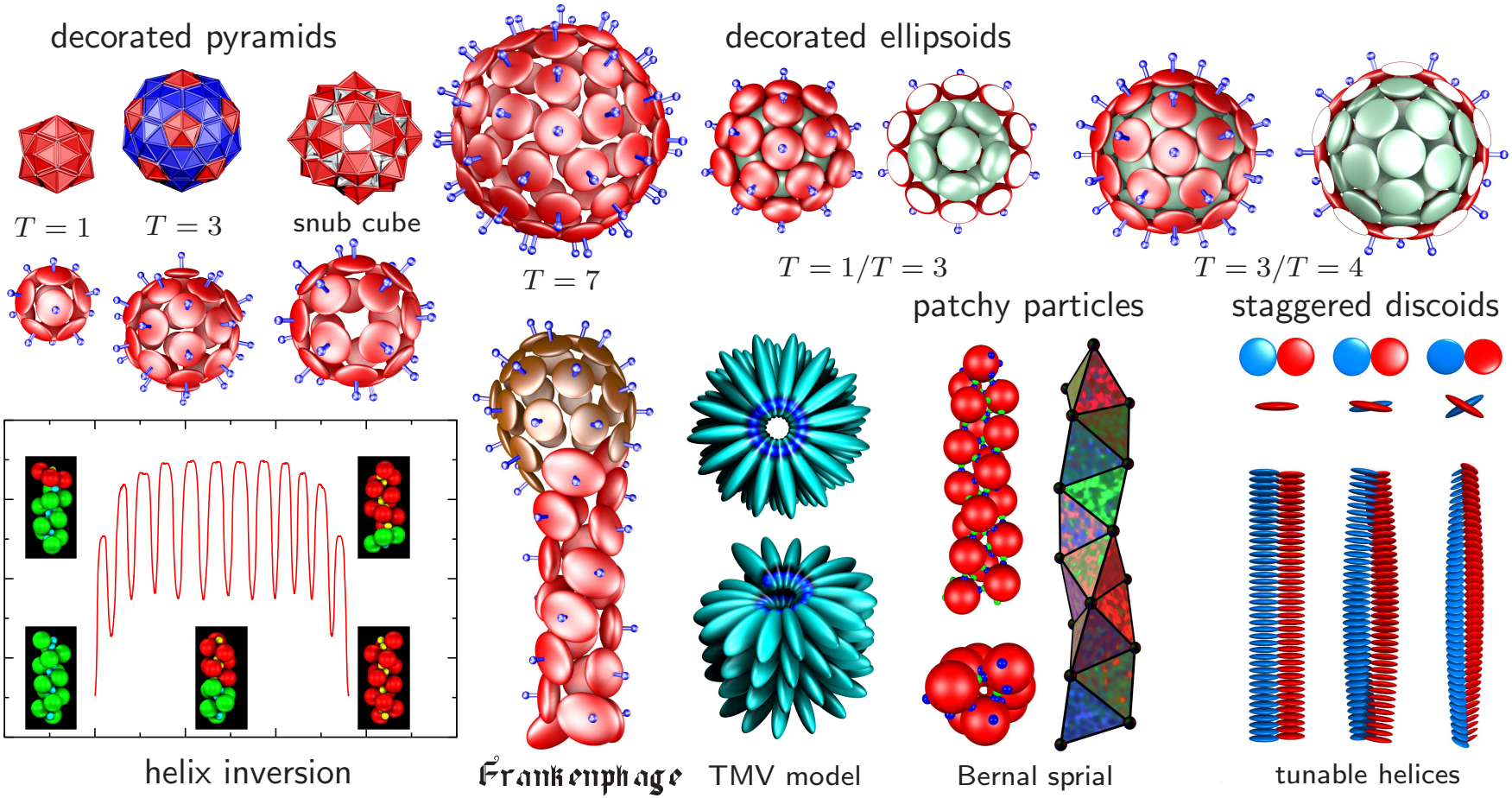

The angle-axis formulation provides a particularly convenient framework for mesoscopic modelling, using both decorated rigid bodies and ellipsoids.

All the terms involving angle-axis coordinates can be obtained by the action of a rotation matrix and its derivatives, which are system-independent.

Emergent Behaviour from Simple Models (*ACS Nano*, **4**, 219, 2010)

Adding two repulsive axial Lennard-Jones sites to an ellipsoidal core produces remarkably versatile building blocks. Oblate ellipsoids favour shells, while stronger repulsion for the longer semiaxis produces tubes and spirals.

Global minima for the oblate ellipsoids include icosahedra for $N = 12$, 32 and 72 ($T = 1, 3$ and 7), the snub cube observed for polyoma virus capsids at $N = 24$, and conical, biaxial, prolate, and oblate shells at other sizes.

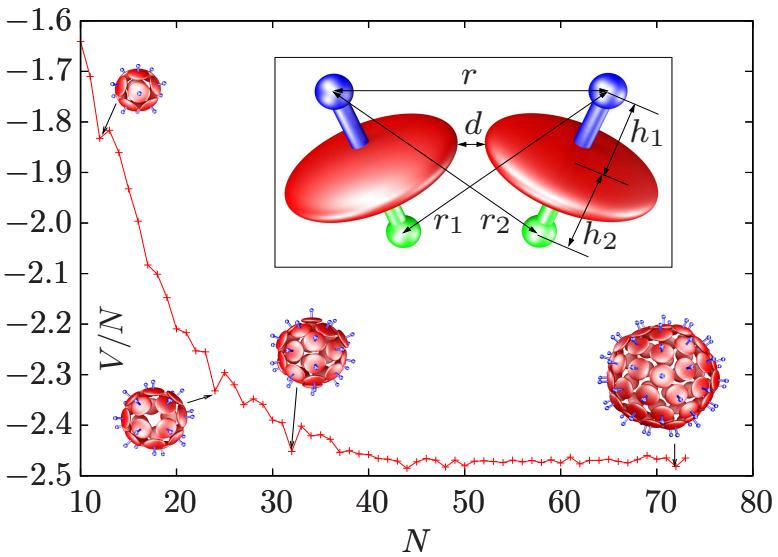

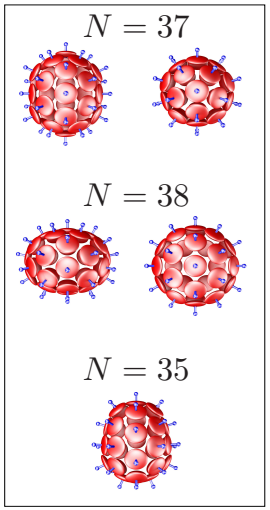

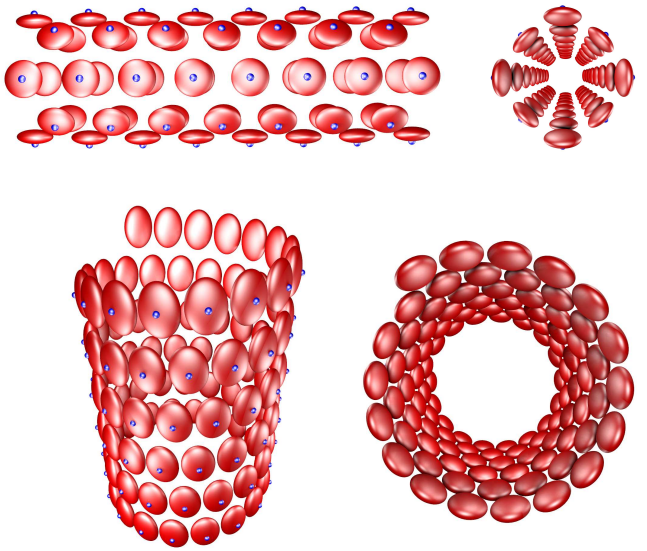

(*ACS Nano*, **4**, 219, 2010)

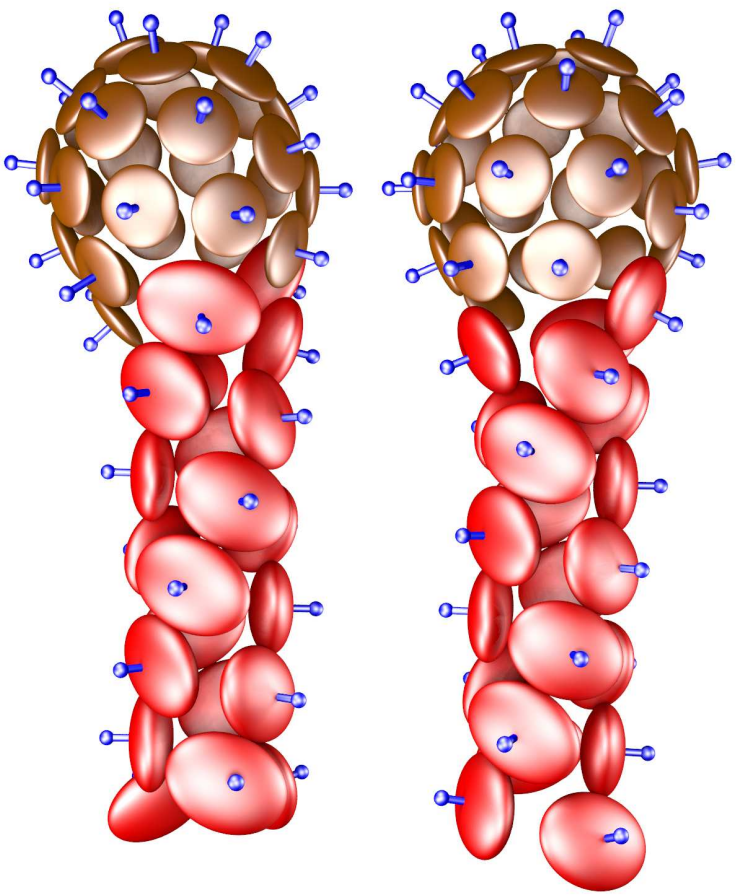

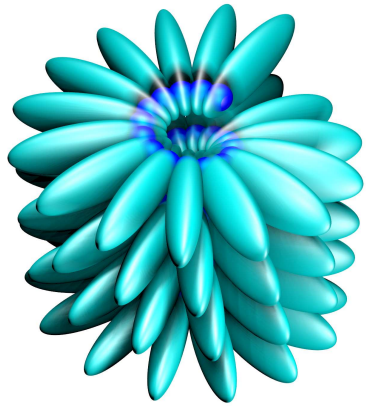

side

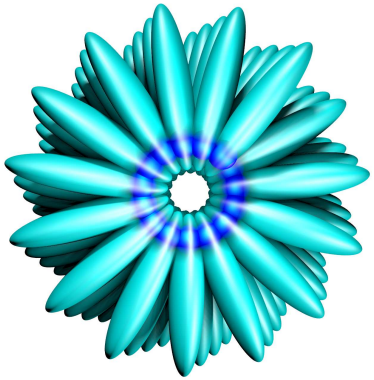

top

Mixing ellipsoidal building blocks that favour shells and tubes produces structures with distinct head and tail regions (left): the .

Particles with a Lennard-Jones site buried in the ellipsoid assemble into a spiral structure (right) with parameters similar to tobacco mosaic virus.

Helical Bilayers From Frustrated Building Blocks (*JPCB*, **117**, 7918, 2013)

helical fibre morphologies

bilayer filaments

magnetic bilayers

Left: introduction of a cytochrome domain into an amyloid fibre can change the morphology from twisted to spiral ribbons and induce systematic kinking.

Centre: rigid building blocks consisting of two ellipsoids can reproduce these structures, which are also observed for Bauhinia seedpods.

Right: the structure depends mostly on the internal geometry of the building blocks, rather than details of the potential. The design principles extend to macroscopic helices formed from elliptical magnets.

Proline Dynamics in Synthetic Collagen Triple Helices

Triple-helical fibrillar collagens have a repetitive G-X-Y sequence in each chain. X and Y are often proline (P) and hydroxyproline (O).

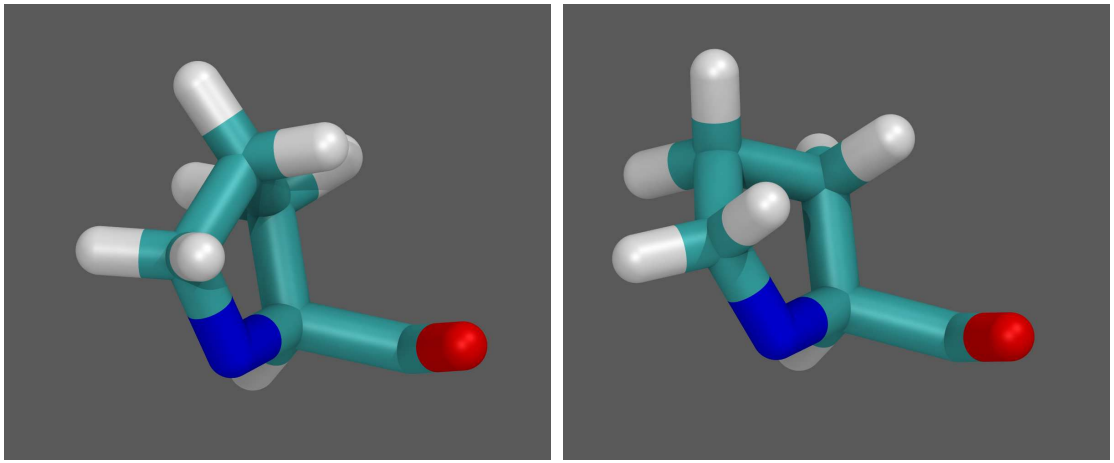

Model peptides feature GPP or GPO triplets; P in the X position (P_X) usually adopts an *endo* conformation (left) whilst P_Y/O_Y tend to be *exo* (right).

ssNMR for labelled mouse bone collagen reveals majority and minority sub-populations for P and G when succeeded by amino or imino residues.

At least 40% of P_X residues in mouse bone prefer the exo conformation.

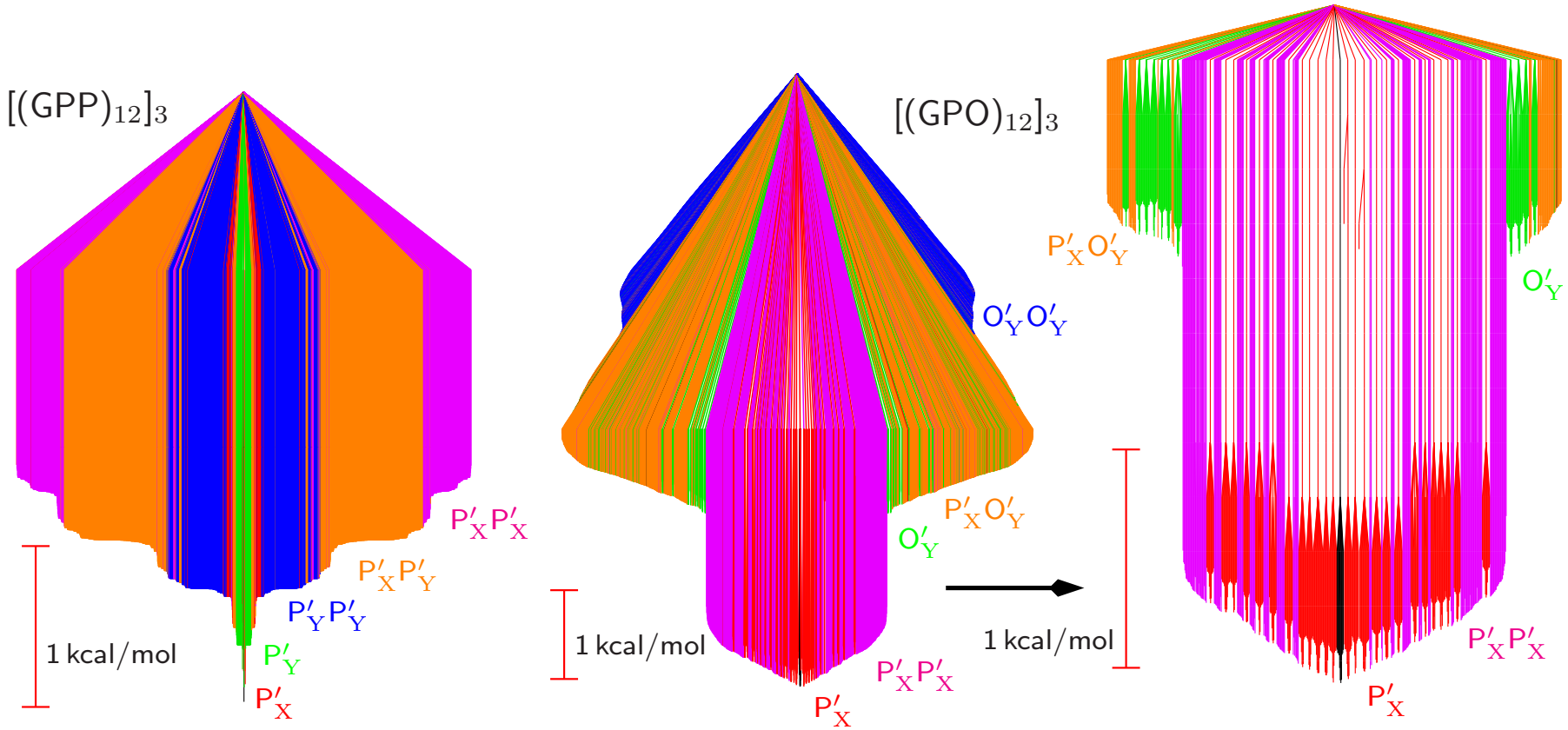

Disconnectivity graphs for single- and double-ring flips (X→X′ etc.) in $[(GPP)_{12}]_3$ and $[(GPO)_{12}]_3$ relative to the global minimum reveal sets corresponding to P'_X, P'_Y, O'_Y, $P'_XP'_X$, $P'_XP'_Y$, $P'_XO'_Y$, $P'_YP'_Y$ and $O'_YO'_Y$.

O in the Y position reduces the energy difference between endo and exo states of prolines in the X position, explaining the latest ssNMR results.

Nanodevices (*Soft Matter*, **7**, 2325, 2011)

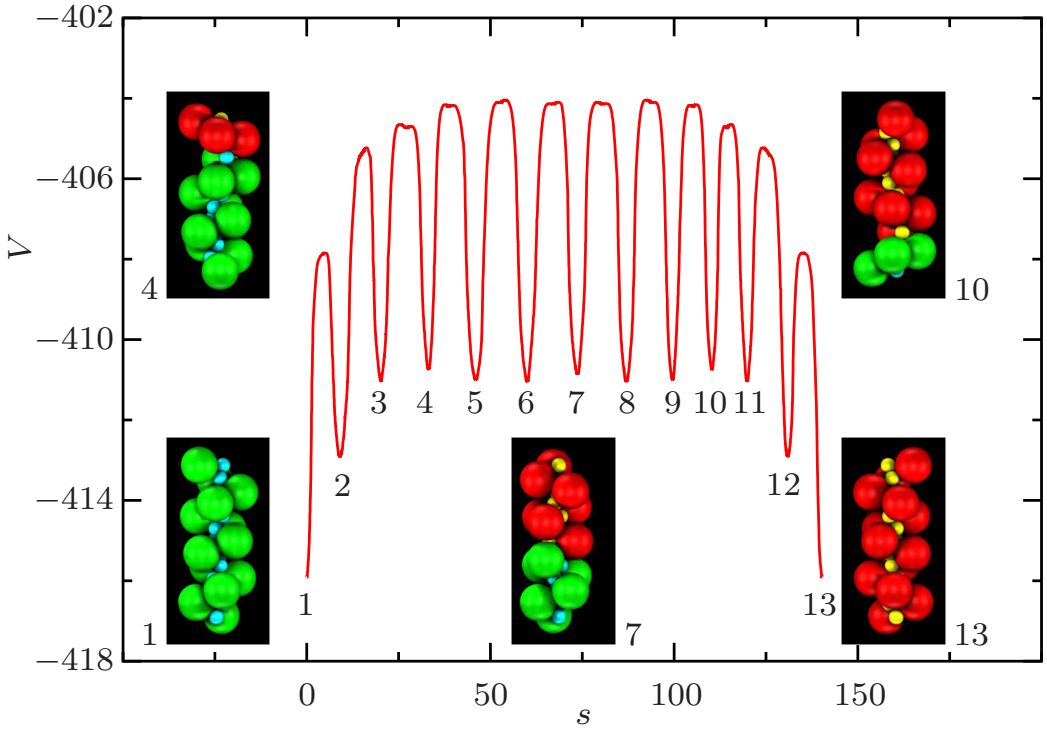

Coupled linear and rotary motion has been characterised for a helix composed of 13 asymmetric dipolar dumbbells in the presence of an electric field.

The helix changes handedness as the boundary between segments propagates along the strand via successive steps that switch the dumbbells.

Designing a Bernal Spiral (*ACS Nano*, **7**, 1246, 2013)

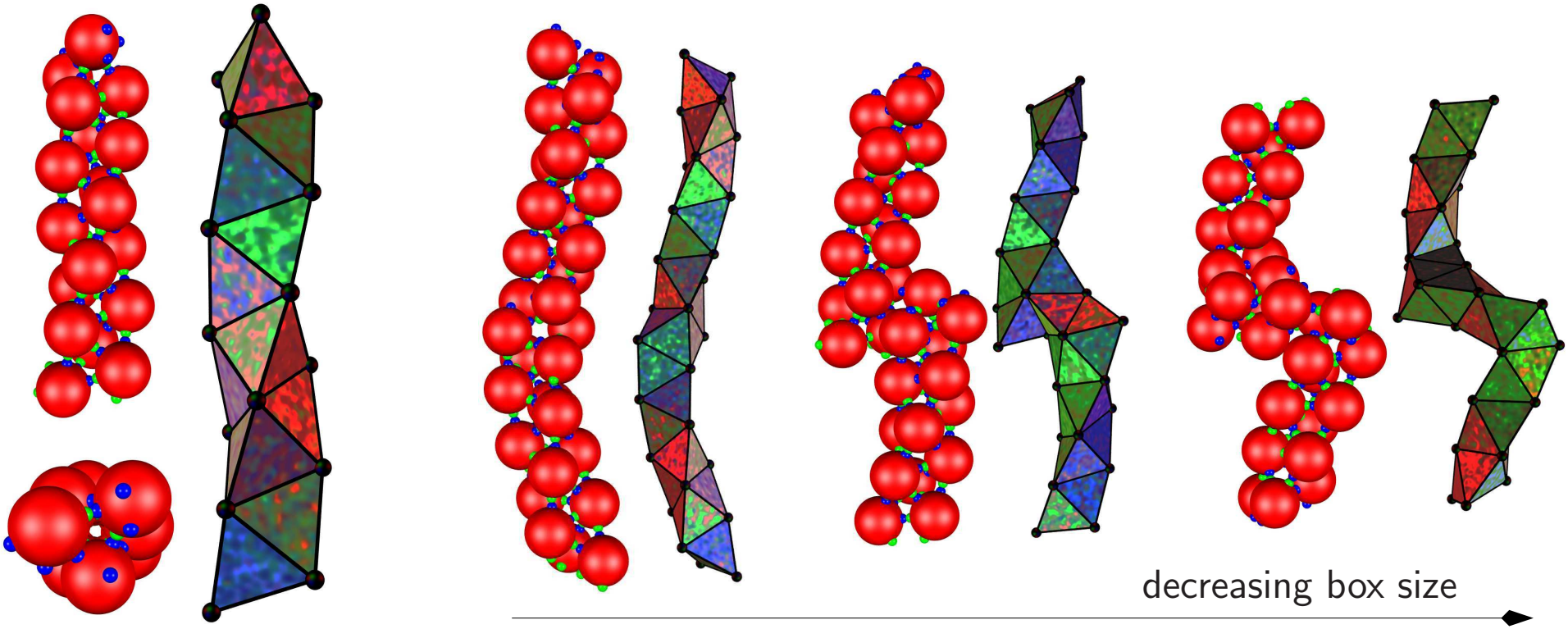

The simplest building blocks that support a Bernal spiral as the global minimum involve a single patch-antipatch pair offset by about 10° from linearity.

Left: Alternative views of a chiral Bernal spiral consisting of 18 particles.

Right: compressed spirals (30 particles, periodic boundaries) exhibit supercoiling or breaks, which resemble structures seen in confocal microscopy.

Folding and Pulling for Protein L and Protein G

Folding pathways and the evolution of the energy landscape as a function of static force have been analysed for protein L and protein G using a sequence-dependent BLN model. B=hydrophobic, L=hydrophilic, and N=neutral.

Protein L forms the N-terminal hairpin 1 first, followed by the C-terminal hairpin 2. The order is reversed for protein G, with an early intermediate.

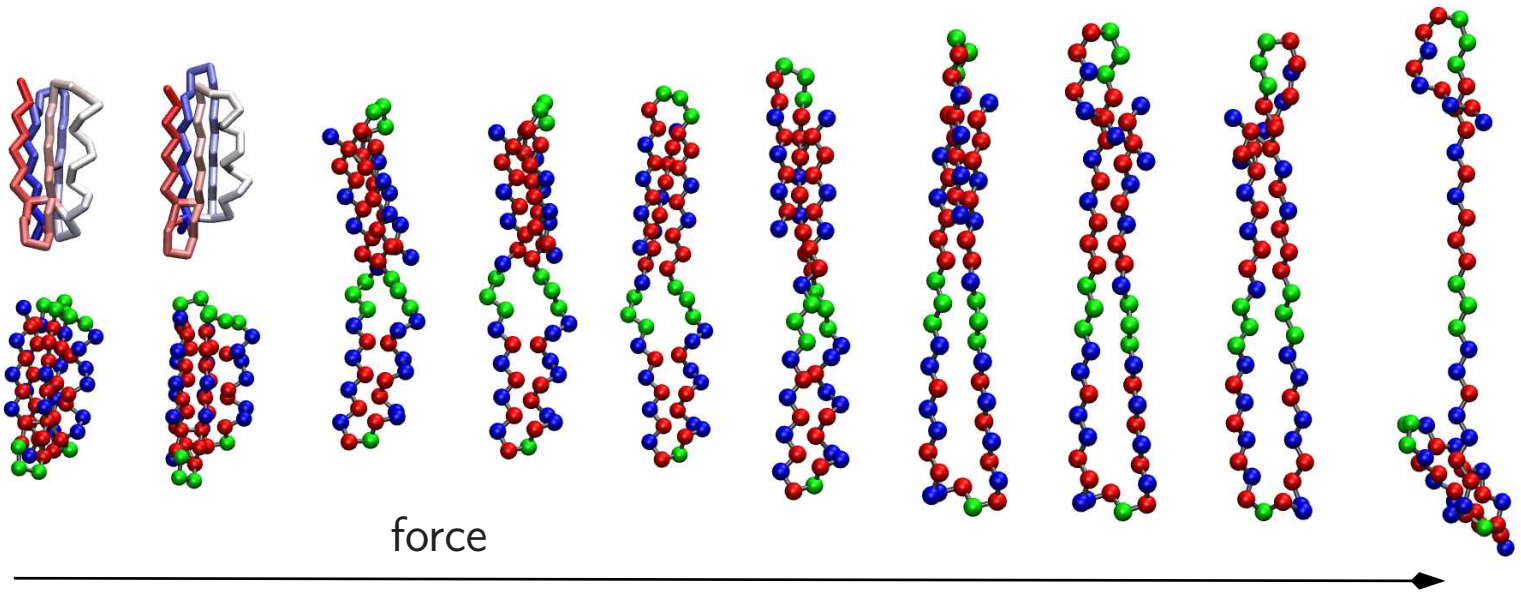

Distinct global minima for protein L as a function of increasing static pulling force applied between beads 10 and 32. (*J. Phys. Chem. B*, **136**, 8394, 2012)

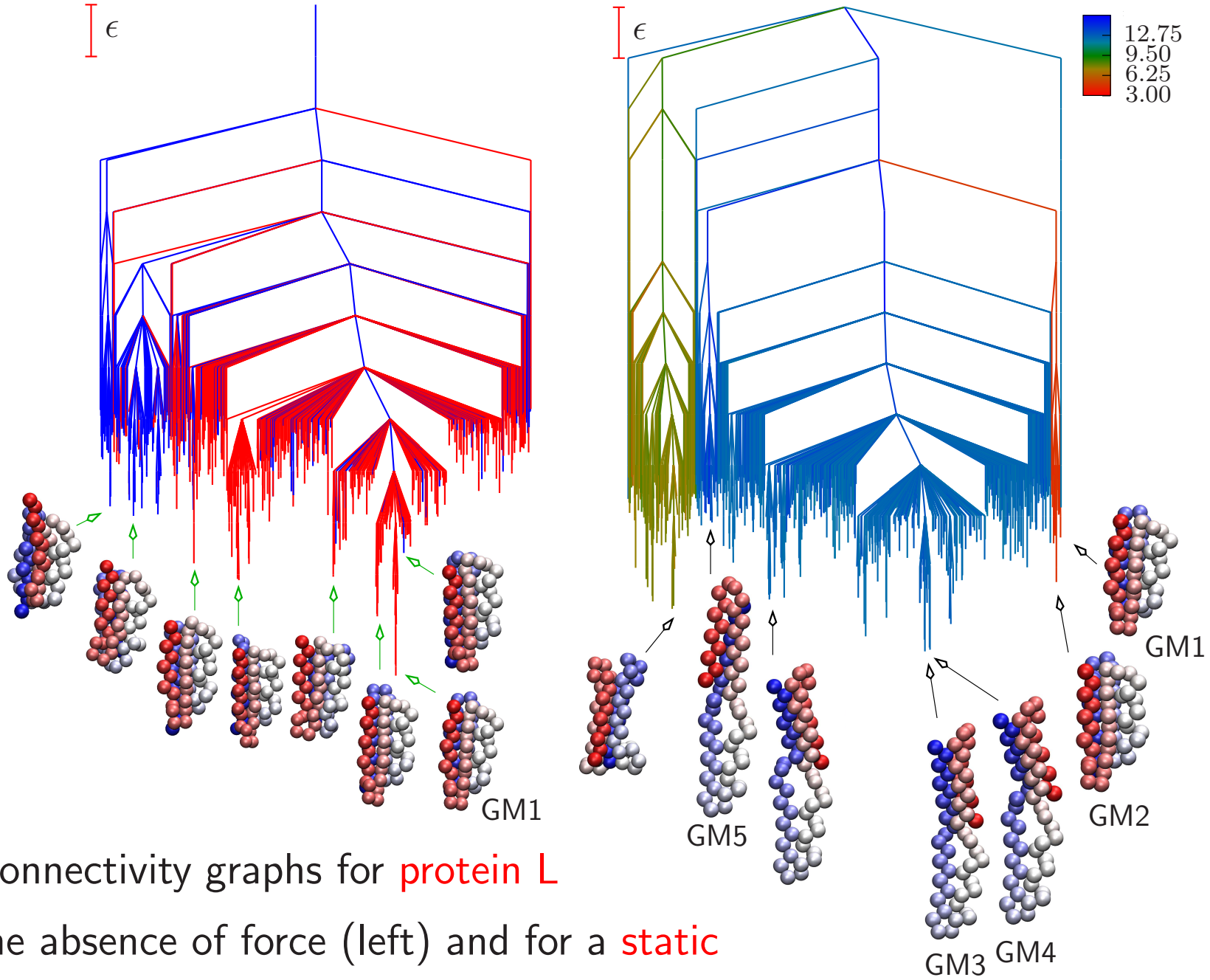

Disconnectivity graphs for protein L in the absence of force (left) and for a static pulling force (right) applied between beads 10 and 32.

Symmetry and Energetics (*Chem. Phys. Lett.*, **285**, 330, 1998; **294**, 262, 2008)

'The symmetry characteristic of a phenomenon is the maximal symmetry compatible with the existence of the phenomenon' (Pierre Curie)

'The perfection of mathematical beauty is such... that whatsoever is most beautiful and regular is also found to be most useful' (D'Arcy Thompson)

However, many systems do not exhibit their highest possible symmetry.

We can write the total energy as a sum over contributions from a many-body expansion, involving single atom, pairwise and three-body terms, etc.

If these terms are drawn from the same distribution then geometrical symmetry (degeneracies) would be manifested as correlation.

The variance is larger when correlation is present. Symmetrical structures are therefore more likely to have particularly high or particularly low energy. Low-lying structures are therefore likely to exhibit symmetry.

More formally, denote the mean and variance of a variable, X, drawn from probability distribution, $p(X)$, as μ and σ^2.

The variance of a sum of N such variables, X_i, is then

$$\mathrm{Var}\left(\sum_{i=1}^{N} X_i\right) = N\sigma^2 + N(N-1)\rho\sigma^2,$$

where the correlation ρ is defined by

$$\rho\sigma^2 = \int (X-\mu)(X'-\mu)p(X,X')dXdX'.$$

For $\rho = 0$ the variance is $N\sigma^2$, but for $\rho = 1$ it rises to $N^2\sigma^2$.

Open question: how should we treat approximate geometrical symmetry, for example, in large biomolecules or condensed matter?

Open question: is it possible to build a more rigorous theory, and make connections with concepts such as designability?

A Modified Superposition Approach (*Chem. Phys. Lett.*, **466**, 105, 2008)

Here the partition function is broken down into contributions from local minima and pathways as a function of an order parameter, a, with terms

$$Z_i(a,T) = \left(\frac{kT}{h\overline{\nu}_i}\right)^{3N-6} \frac{\exp\left(-V_i/kT\right)}{\sqrt{2\pi kTA_i}} \exp\left[-\frac{(a-a_i)^2}{2kTA_i}\right],$$

where A_i is a weighted sum of order parameter derivatives.

Free energy surfaces for alanine dipeptide (CHARMM22/vacuum) from superposition, replica exchange, and reaction path Hamiltonian superposition:

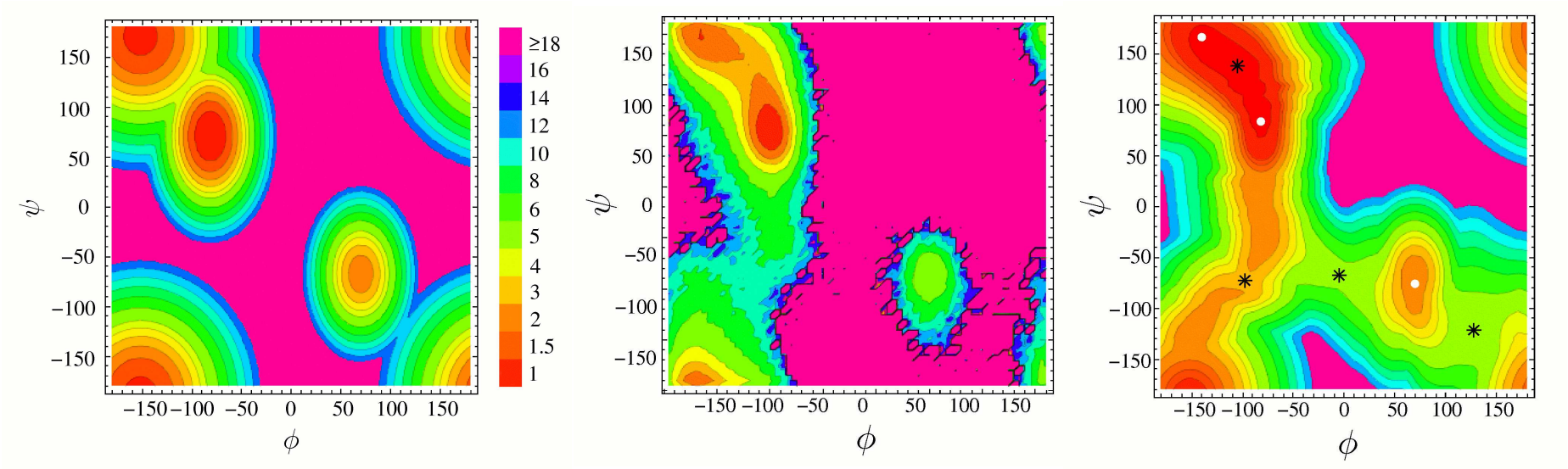

Thermodynamics for Ala_4 in Vacuum: CHARMM

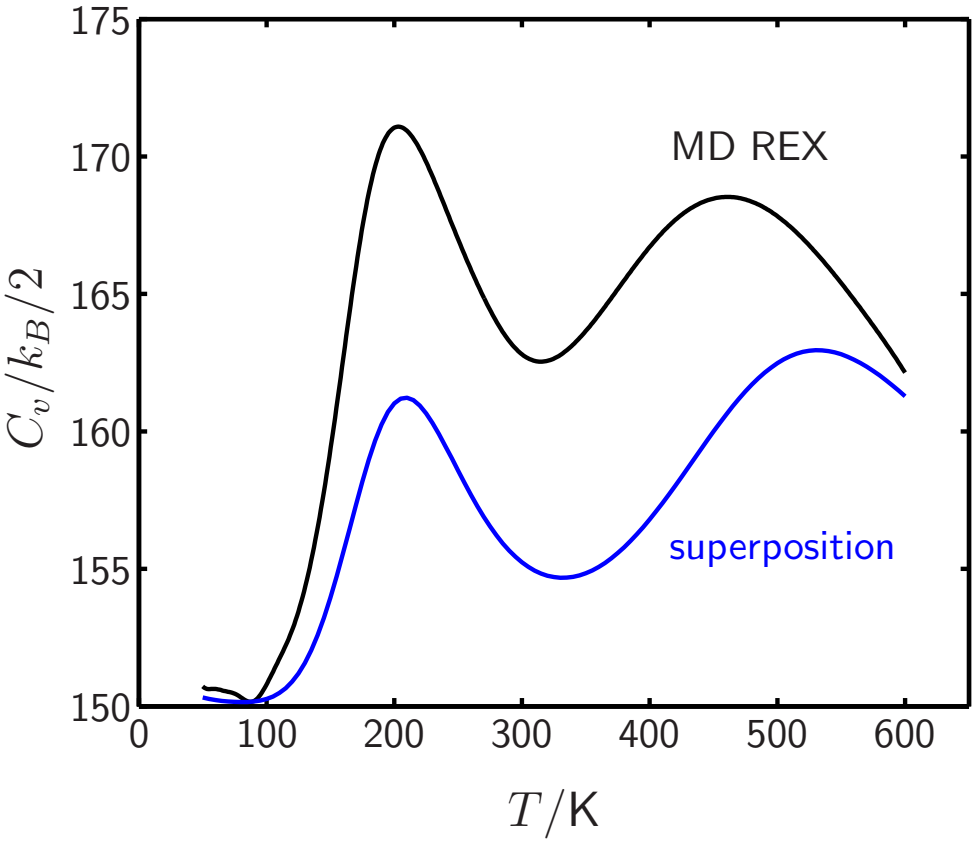

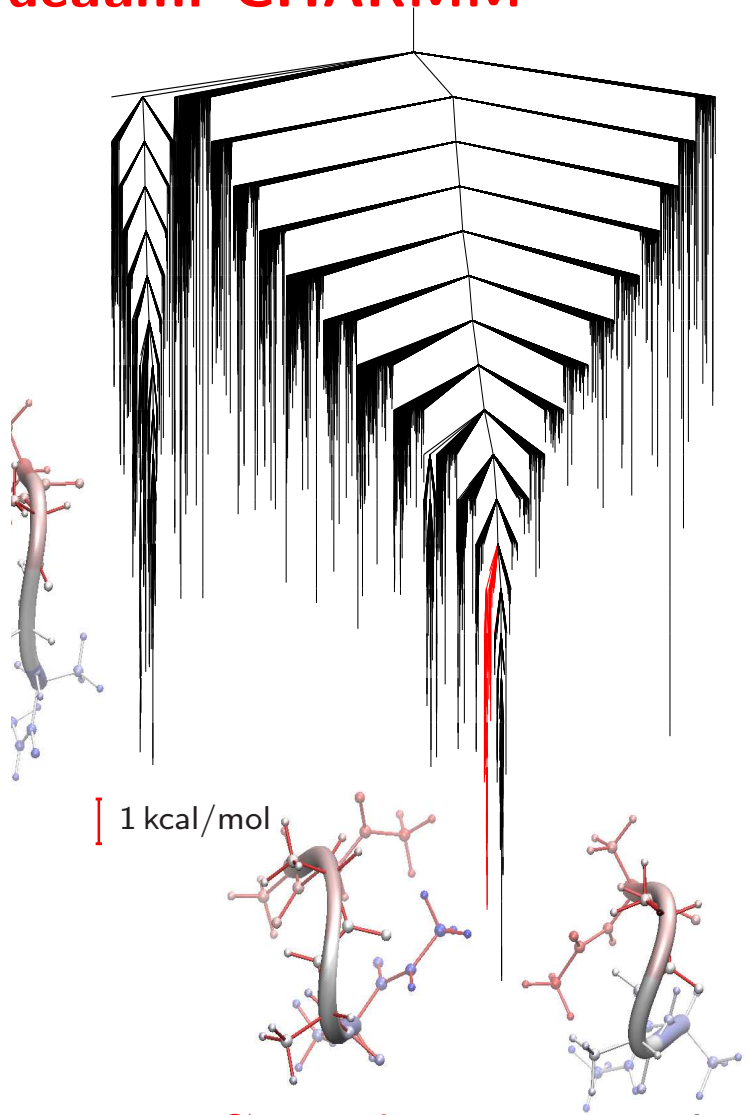

Ala_4 in vacuum (charmm27) has a low temperature C_v peak, corresponding to the hundred or so lowest minima in the disconnectivity graph. The high temperature peak corresponds to the finite system analogue of melting.

Thermodynamics for Ala_4 in Vacuum: AMBER

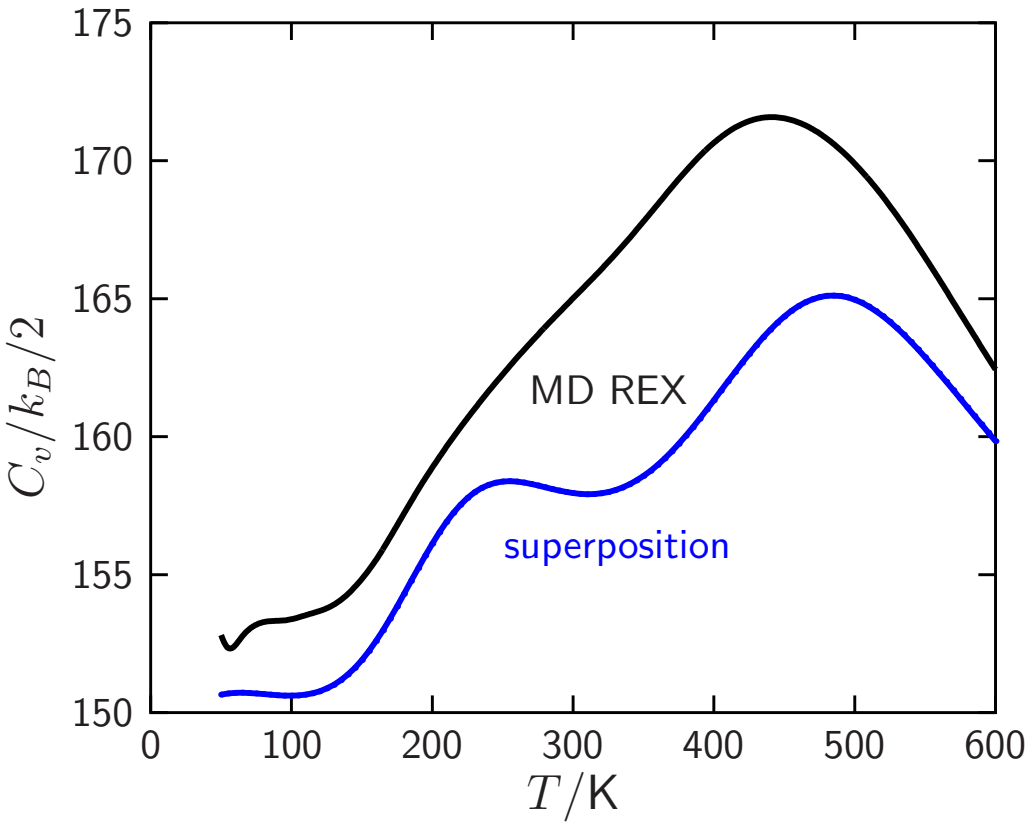

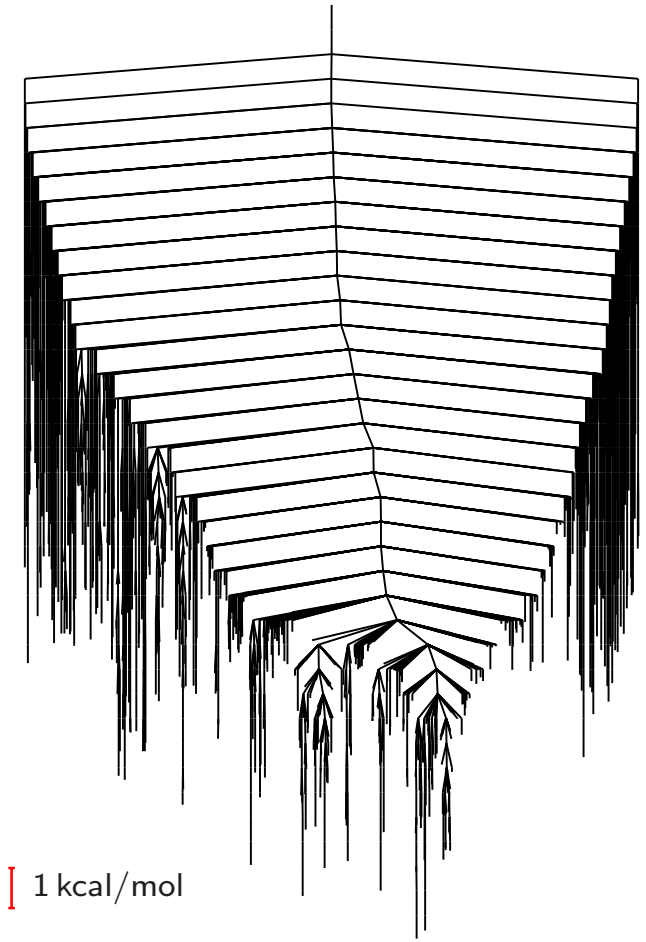

Replica exchange (REX) and superposition results for the heat capacity C_v of ala_4 in vacuum (amber99sb) appear similar to CHARMM. (*J. Chem. Phys.*, **139**, 121909, 2013)

Thermodynamics for Ala_4 in Vacuum: AMBER

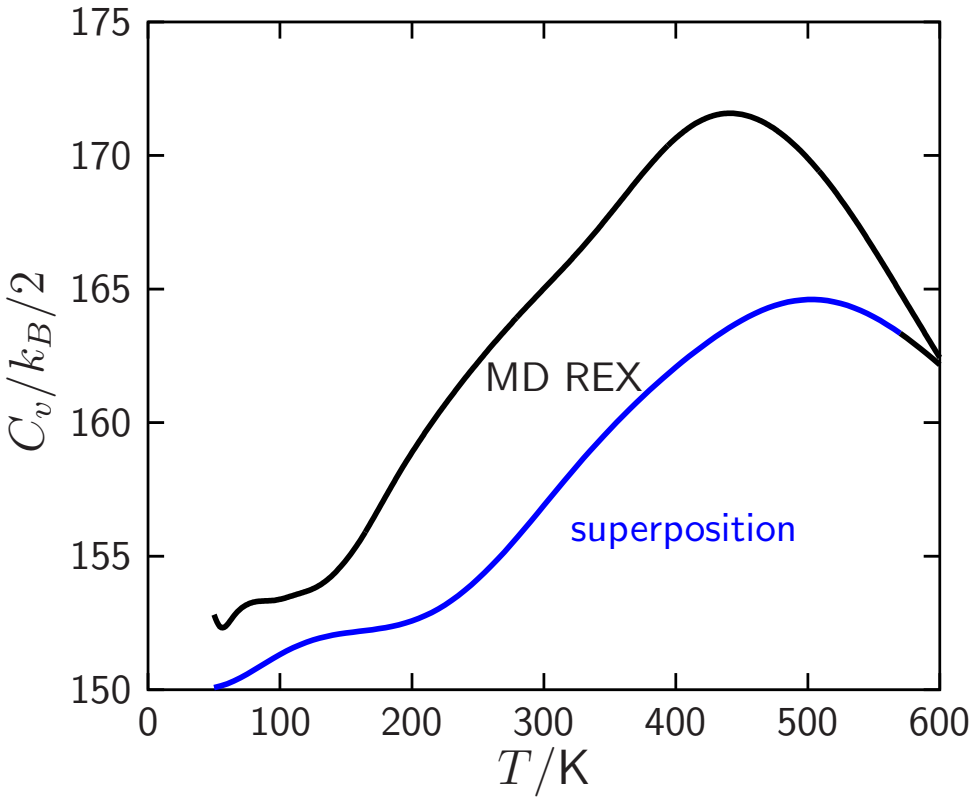

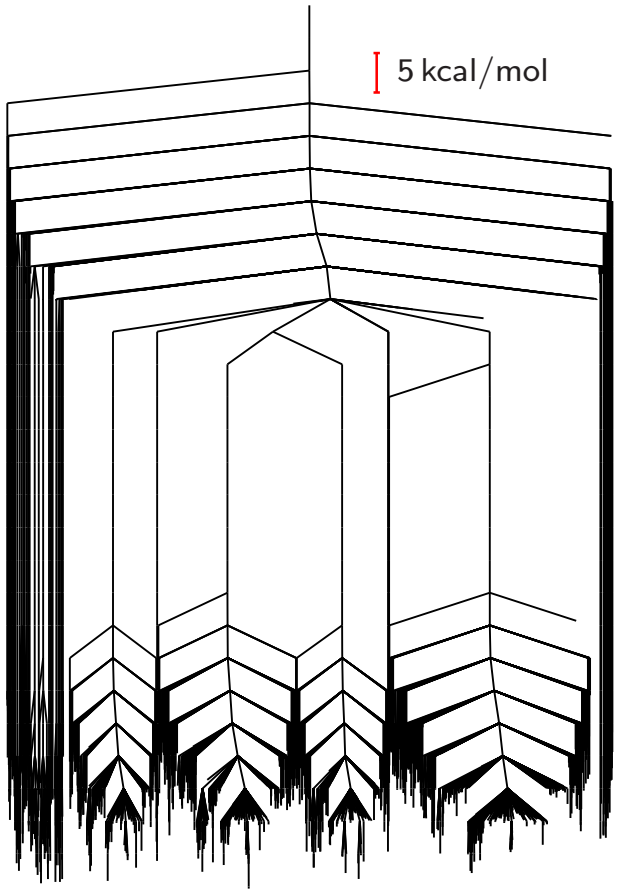

The global minimum for this potential has a mixture of L and D amino acids. The landscape separates into regions with different L/D composition, spearated by barriers of order 90 kcal/mol. (*J. Chem. Phys.*, **139**, 121909, 2013)

Energy Landscapes for the P46 Model Protein (*JCP*, **111**, 6610, 1999)

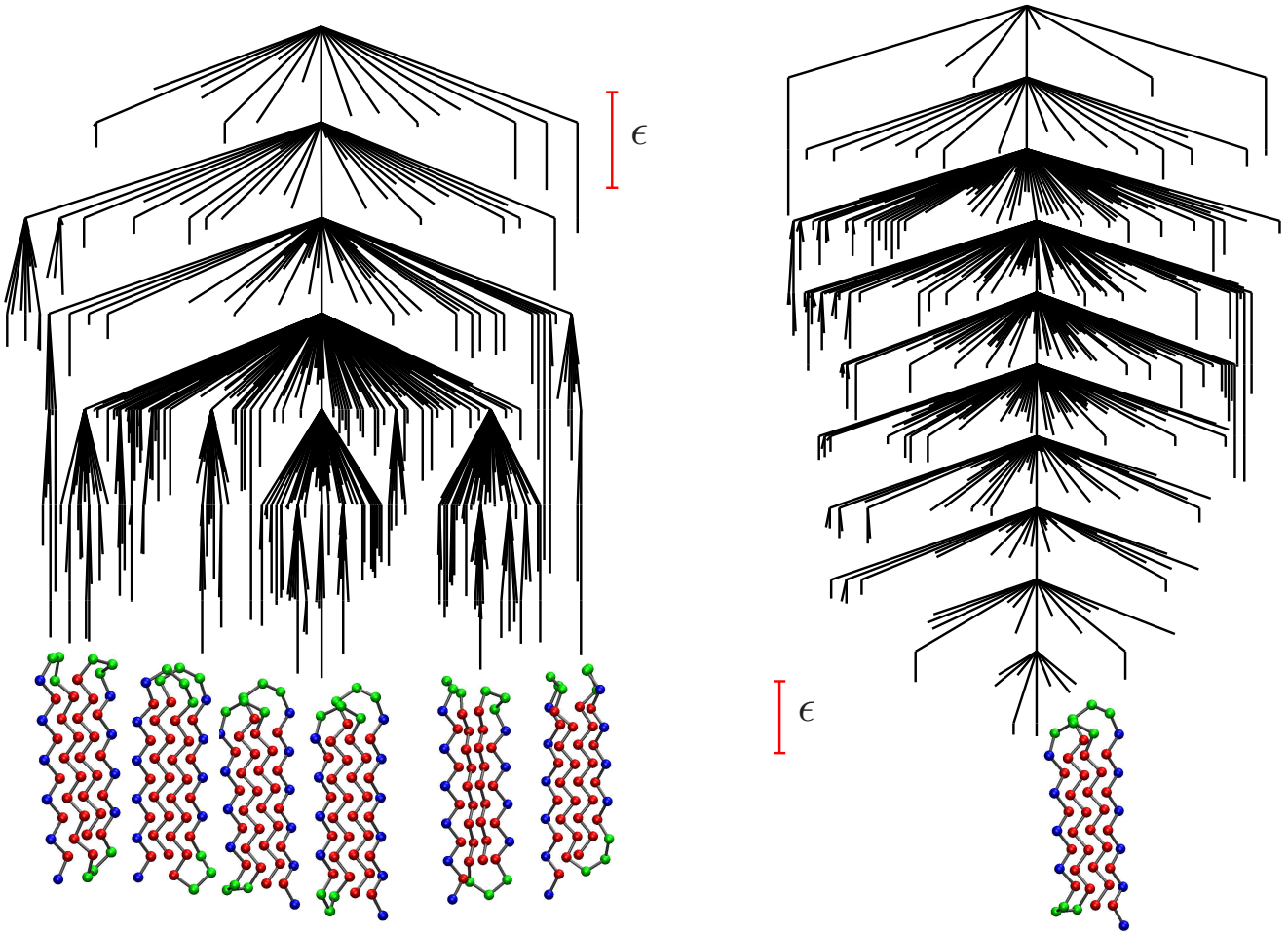

The global minimum of the off-lattice bead model $\mathrm{B_9N_3(LB)_4N_3B_9N_3(LB)_5L}$ is a four-stranded β-barrel, where B=hydrophobic, L=hydrophilic, and N=neutral. The original system exhibits frustration, which is eliminated in the corresponding Gō model [and reduced by salt bridges (*JCP*, **121**, 10284, 2004)].

Glassy Landscapes (*J. Chem. Phys.*, **129**, 164507, 2008)

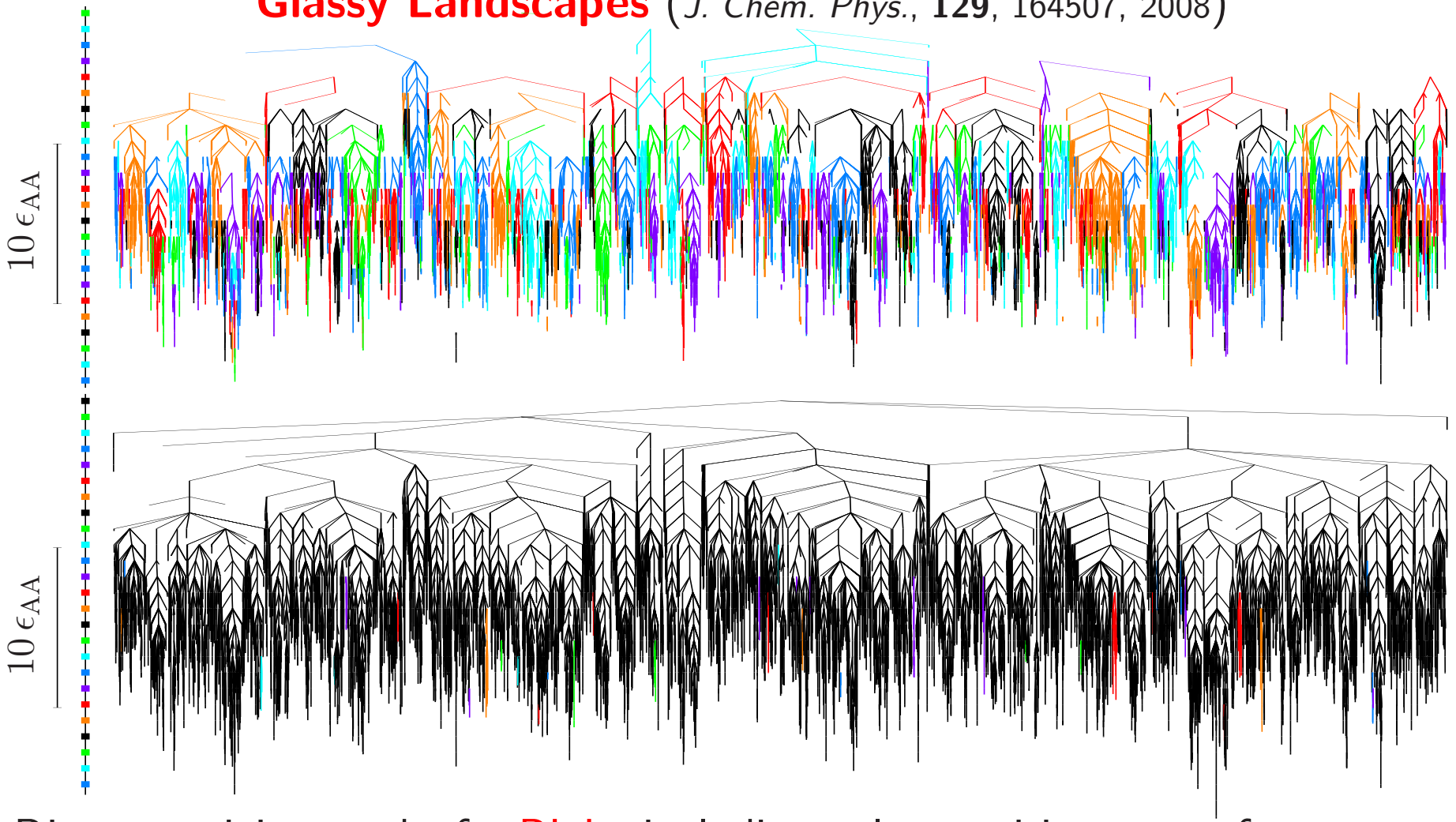

Disconnectivity graphs for BLJ_{60} including only transition states for noncage-breaking (top) and cage-breaking (bottom) paths. Changes in colour indicate disjoint sets of minima. Cage-breaking transitions, defined by two nearest-neighbour changes, define a higher order metabasin structure.

The Ring-Polymer Instanton Approach (*JCP*, **131**, 214106, 2009)

The ring polymer approximation to the quantum partition function $Q(\beta) = \mathrm{trace}\left[e^{-\beta\hat{H}}\right]$ is obtained by a Trotter factorisation into P imaginary time steps of length $\beta\hbar/P$. For particles of mass m and $\mathbf{x} = \{\mathbf{x}_1, \ldots, \mathbf{x}_P\}$:

$$Q(\beta) \approx \left(\frac{mP}{2\pi\beta\hbar^2}\right)^{P/2} \int e^{-\beta U_P(\beta,\mathbf{x})/P}\, d\mathbf{x},$$

$$\text{with} \qquad U_P(\beta,\mathbf{x}) = \sum_{\alpha=1}^{P} V(\mathbf{x}_\alpha) + \frac{mP^2}{2\beta^2\hbar^2} \sum_{\alpha=1}^{P} (\mathbf{x}_\alpha - \mathbf{x}_{\alpha+1})^2,$$

a mapping onto a classical ring polymer with P beads, each corresponding to a configuration of the physical system and coupled by harmonic springs.

Transition states of $U_P(\beta,\mathbf{x})$ represent a finite-difference approximation to periodic instanton pathways. This approach provides approximate tunneling splittings with all degrees of freedom treated quantum mechanically.

Regrouping Stationary Point Databases

Lumping local minima together (recursively) if they are separated by low barriers or fast rates reduces the dimension of the kinetic transition network (*J. Chem. Phys.*, **123**, 234901, 2005; *J. Chem. Phys.*, **121**, 1080, 2004). It also provides a self-consistent definition of products and reactants.

The occupation probability and free energy of a group of minima, J are

$$p_J^{\mathrm{eq}}(T) = \sum_{j \in J} p_j^{\mathrm{eq}}(T) \quad \text{and} \quad F_J(T) = -kT \ln \sum_{j \in J} Z_j(T),$$

and the free energy of the transition states connecting J and L is then

$$F_{LJ}^{\dagger}(T) = -kT \ln \sum_{(lj)^{\dagger}} Z_{lj}^{\dagger}(T), \qquad l \in L,\ j \in J,$$

$$\text{with} \quad k_{LJ}^{\dagger}(T) = \sum_{(lj)^{\dagger}} \frac{p_j^{\mathrm{eq}}(T)}{p_J^{\mathrm{eq}}(T)} k_{lj}^{\dagger}(T) = \frac{kT}{h} \exp\left[-\frac{\left(F_{LJ}^{\dagger}(T) - F_J(T) \right)}{kT} \right].$$

Finding an Initial Discrete Path for Distant Minima

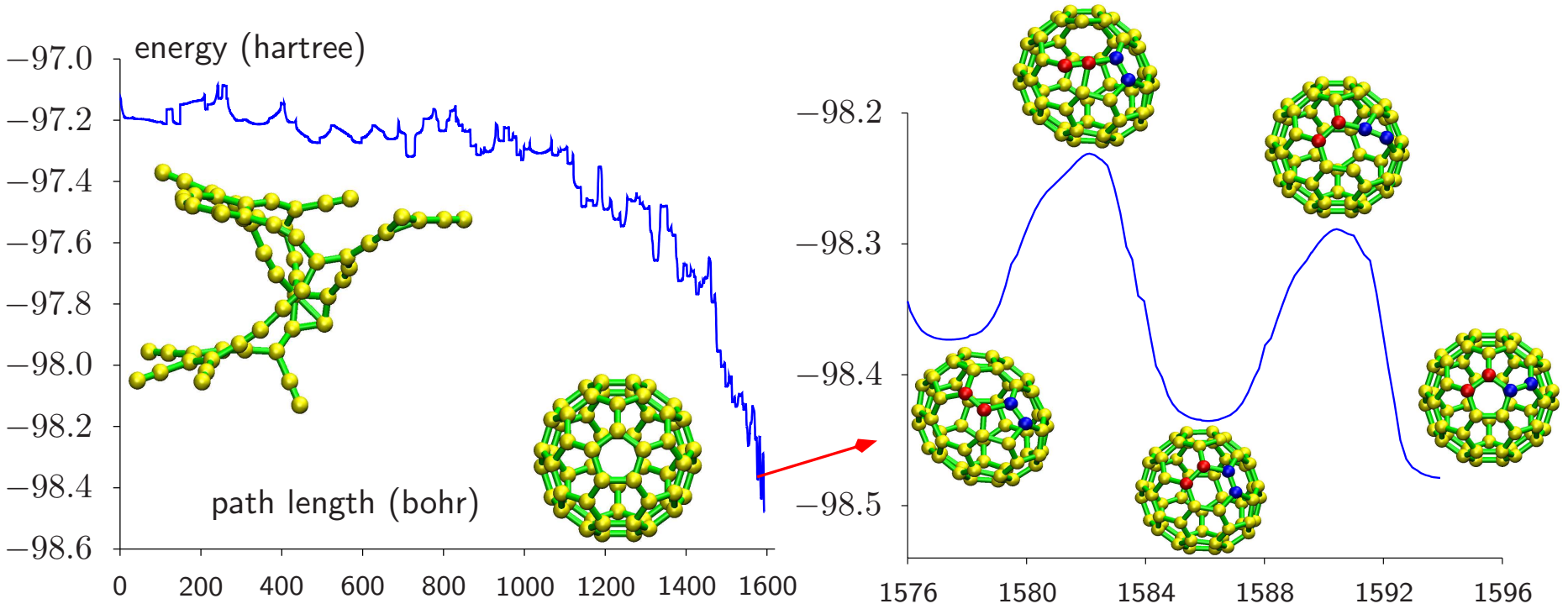

Distant local minima can be connected by successive transition state searches using Dijkstra's algorithm to choose the next pair of minima, avoiding a combinatorial problem (*J. Chem. Phys.*, **122**, 234903, 2005).

This C_{60} path from a random network to buckminsterfullerene contains 82 transition states, and required 383 cycles of the Dijkstra missing connection algorithm, including 1620 DNEB searches, for a tight-binding potential.

The minima can be used to define a complete graph with edge weights

$$w(u,v) = \begin{cases} 0, & \text{if } u \text{ and } v \text{ are connected by one transition state,} \\ \infty, & \text{if } n(u,v) = n_{max}, \\ f(D(u,v)), & \text{otherwise,} \end{cases} \tag{1}$$

where $n(u,v)$ is the number of times pair (u,v) was selected for a connection attempt, n_{max} is the maximum number of attempts, and $D(u,v)$ is the minimum Euclidean distance between u and v. f should be a monotonically increasing function, such as $f(D(u,v)) = D(u,v)^2$.

Dijkstra's algorithm (*Numerische Math.*, **1**, 269, 1959) can now determine the shortest path between any minima. If the weight of the pathway is non-zero, it contains one or more 'gaps', which are then chosen as DNEB end points.

The computational complexity is at worst quadratic in the number of minima, and the memory requirements scale in a similar fashion.

$N^{\rm st}$ Increases Exponentially (*PRA*, **25**, 978, 1982; *JCP*, **116**, 3777, 2002)

A simple theory suggests a power law for the number of local minimum energy structures, $M^{\rm st}_{\rm min}(N)$, as a function of the number of atoms, N.

If the system is large enough so that it can be divided into m equivalent subsystems of N atoms each, and the subsystems are independent, then

$$M^{\rm st}_{\rm min}(mN) = M^{\rm st}_{\rm min}(N)^m \qquad \text{so that} \qquad M^{\rm st}_{\rm min}(N) = \exp(\epsilon N).$$

If the rearrangement corresponding to a transition state is localised in one subsystem, then a transition state of the mN-atom system occurs when one of the subsystems is at a transition state and the rest are at a minimum, so

$$M^{\rm st}_{\rm ts}(mN) = m\, M^{\rm st}_{\rm min}(N)^{m-1} M^{\rm st}_{\rm ts}(N) \qquad \text{and} \qquad M^{\rm st}_{\rm ts}(N) = N \exp(\epsilon N).$$

The ratio $M^{\rm st}_{\rm ts}/M^{\rm st}_{\rm min}$ is therefore predicted to grow linearly with size, in reasonable agreement with numerical results for small Lennard-Jones clusters.

The positive scaling parameter ϵ is larger for short-ranged potentials.

Connecting Dynamics and Thermodynamics (*Science*, **293**, 2067, 2001)

The organisation of a PES is governed by its stationary points, where Taylor expansions provide local descriptions in terms of Hessian matrices.

The organisation of families of PES's as a function of parameters in the potential is determined by the stationary points that possess additional zero Hessian eigenvalues, known as non-Morse points.

Catastrophe theory provides a local representation of the PES around non-Morse points as a function of both atomic coordinates and parameters.

The splitting lemma reduces the dimensionality to the essential variables, while transversality guarantees that the resulting classifications are universal.

The simplest one-parameter catastrophes are the fold, $f(x) = \frac{1}{3}x^3 + ax$, and the symmetrical cusp, $f(x) = \frac{1}{4}x^4 + \frac{1}{2}ax^2$.

Geometries of the fold and cusp catastrophes.

curvature$= -\lambda$

fold: $r_{\mathrm{f}} = \dfrac{6\Delta V}{\lambda \Delta s^2} = 1$

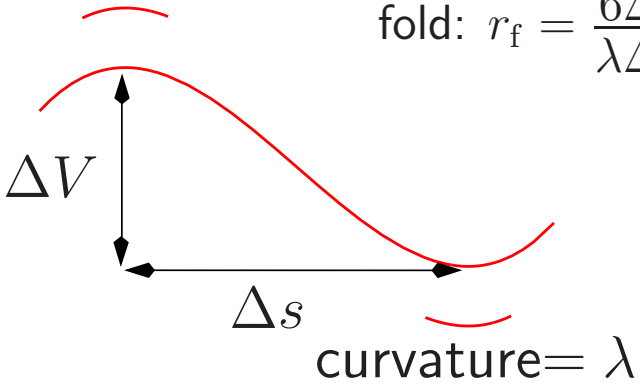

curvature$= \lambda$

curvature$= -2\lambda$

cusp: $r_{\mathrm{c}} = \dfrac{4\Delta V}{\lambda \Delta s^2} = 1$

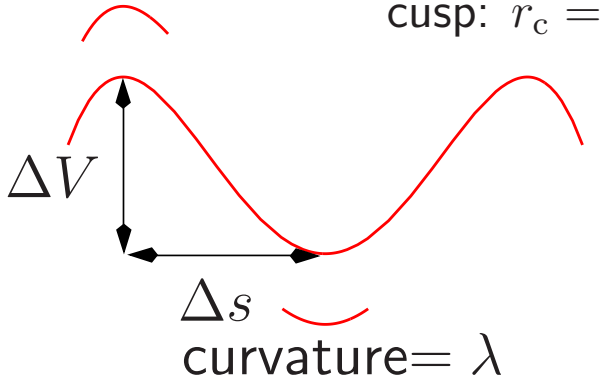

curvature$= \lambda$

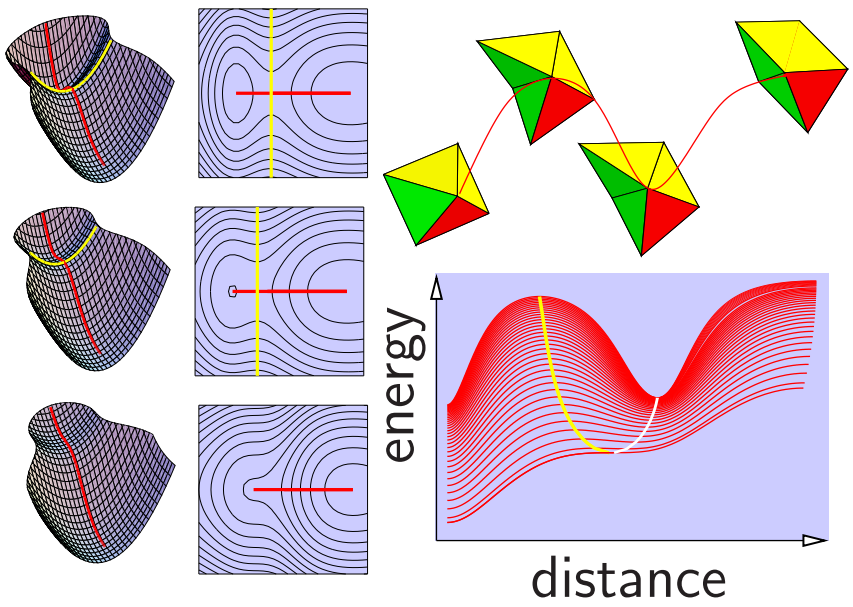

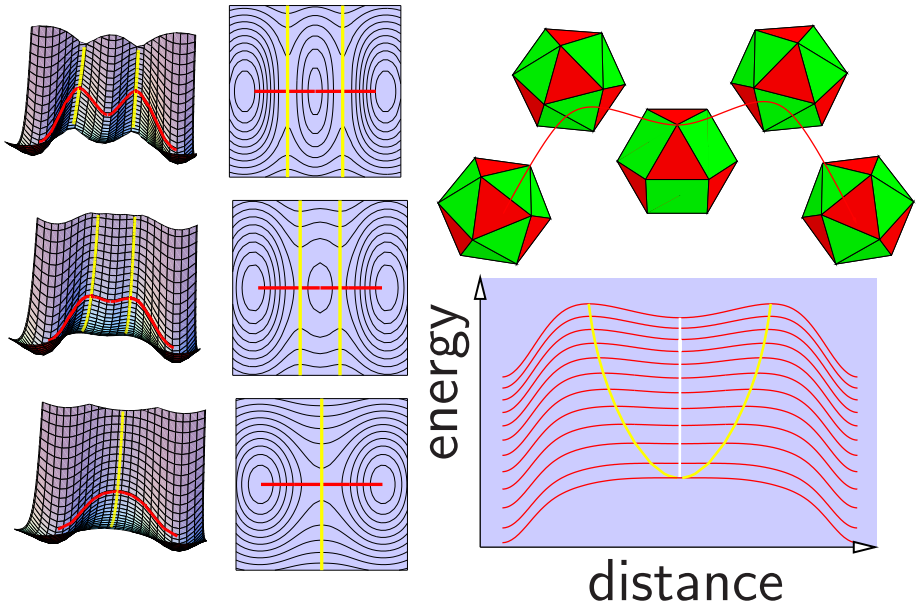

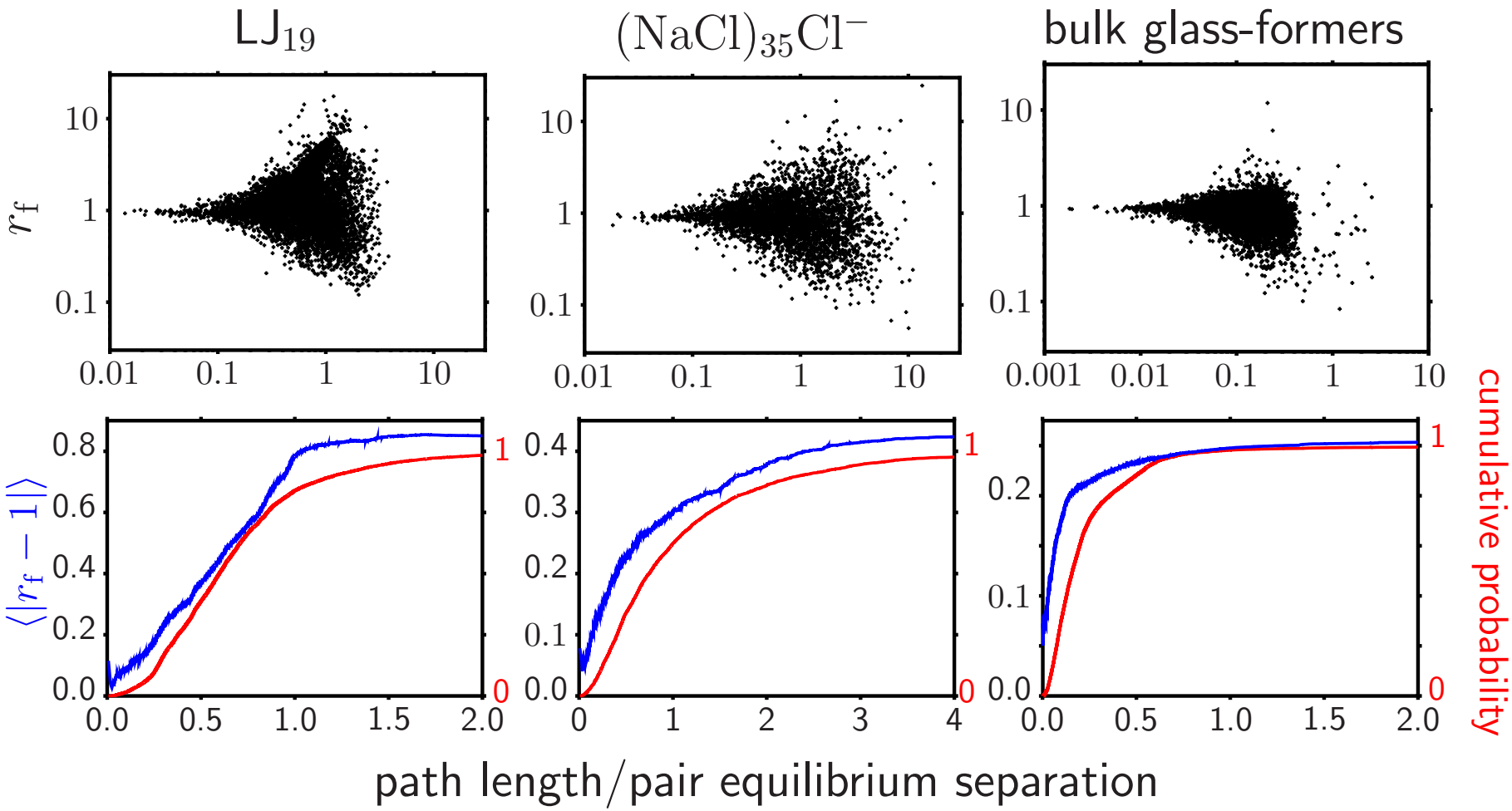

For systems with a fixed potential we effectively have a snap-shot of parameter space. On average, r_{f} remains close to unity for many pathways in both model clusters and bulk, providing an explanation for Hammond's postulate.